Desalination and Water Treatment
www.deswater.com

doi: 10.5004/dwt.2017.20463

71 (2017) 116–135
April

Removal of some types of polyphenols and aromatic amines in textile industry wastewaters by nanocerium-dioxide-doped titanium dioxide

Delia Teresa Sponza*, Rukiye Oztekin

Department of Environmental Engineering, Engineering Faculty, Dokuz Eylül University, Tınaztepe Campus, 35160 Buca/Izmir, Turkey, Tel. +90 232 301 7119; Fax: + 90 232 453 11 43; emails: delya.sponza@deu.edu.tr (D.T. Sponza), rukiyeoztekin@gmail.com (R. Oztekin)

Received 2 June 2016; Accepted 26 December 2016

ABSTRACT

The interfacial and surface structures of CeO_2-doped TiO_2 prepared under laboratory conditions have been investigated in detail by means of X-ray diffraction (XRD), Brunauer–Emmett–Teller (BET) surface area measurement, a high-resolution transmission electron microscope, X-ray photoelectron spectroscopy (XPS) and energy-dispersive spectroscopy (EDS). TiO_2 and CeO_2 are in the anatase phase and the cubic-fluorite phase in CeO_2–TiO_2 mixed oxides, respectively. The mixed CeO_2–TiO_2 nanocomposite exhibits much higher surface areas than the individual oxides. Field-emission scanning electron microscope analysis showed that TiO_2 exhibited aggregated spherical particles while a flake-like shape was observed for CeO_2. The peak locations and relative intensities in XRD showed cubic-fluorite crystalline structure for CeO_2. BET analysis results showed that the maximum surface area and pore volume were obtained at a CeO_2 ratio of 15 mg/L CeO_2-doped TiO_2 nanocomposite. The energy dispersive spectrum of the CeO_2-doped TiO_2 nanocomposite showed that only Ti, Ce and O elements are detected in the CeO_2-doped TiO_2 nanocomposite and Ce is mixed with TiO_2. Maximum color, polyphenols (quercetin, fisetin, ellagic acid, carminic acid, luteolin and curcumin) and polyaromatics (2,6-dimethylaniline, 2-aminoanisole, 2,4-toluenediamine, 4,40-thiobisbenzenamine and 3,3-dichlorobenzidine) removal efficiencies were observed between 97% and 99% in a textile industry wastewater (TI ww) treatment plant located in Izmir, Turkey, during photodegradation experiments, under 130 W UV light, at 15% CeO_2 containing 15 mg/L CeO_2-doped TiO_2 nanocomposite, at 21°C, after 30 min irradiation time. The results show that the CeO_2/TiO_2 nanocomposite produced has a high photocatalytic activity to remove pollutants from TI ww.

Keywords: Cerium-dioxide-doped titanium dioxide; Nanocomposite; Polyaromatics; Polyphenols; Textile industry wastewater

1. Introduction

Textile industries generate a number of pollutants, which they discharge to the surrounding environment without any further treatment [1]. These pollutants not only add color to water but also cause extensive toxicity to aquatic and other forms of life [2]. About 10%–15% of the total dyes from various textile and other industries get discharged in wastewater causing extensive pollution [1,2]. Therefore, the treatment of industrial effluents containing polyaromatic and polyphenolic compounds becomes necessary prior to their final discharge to the environment. Conventional methods for the effective removal of phenols, polyphenols, aromatic amines and dyes are outdated due to certain inherent limitations that they have [3]. The recalcitrant nature of textile effluents largely containing high concentrations of dyestuffs, salts, acids, bases, surfactants, dispersants, humectants, oxidants and detergents renders these waters aesthetically unacceptable and unusable. Textile dyes are well-known mutagens and carcinogens posing risks to various ecosystems, animals' health and agriculture [4]. Therefore, the treatment of these high volumes of wastewater becomes crucial. Available techniques such as physical and

* Corresponding author.

biological adsorption, membrane filtration, oxidation, ozonation and microbial biodegradation are generally employed for remediation of dye containing effluents. These treatment and removal practices are not always followed as per the governing standards and thus ultimately cause serious pollution. These approaches are expensive and unaffordable for small-scale industries and processors [5].

It was shown that the complex structures of amino-azo benzene dyes and their various derivatives may lead to mutagenesis, which is a major cause of cancer [6]. The International Agency for Research on Cancer (IARC) has declared benzidine-like dyes to be extremely powerful carcinogens to many mammals and, alarmingly, human beings [7]. Experiments on Swiss albino rats as model organisms have shown the toxicity of textile wastewater to animals [8]. The textile industry wastewater (TI ww) effluents are characterized by alkaline reaction, significant salinity, intensive color and toxicity [9]. As a result, colored wastewater is emitted to the aquatic environment, where it creates problems for photosynthetic aquatic plants and algae [10–12]. Some of them or their degradation products are toxic, mutagenic or cytotoxic [13–15].

In the treatment of TI ww it is impossible to obtain satisfactory effects using only one of them; the integration of different processes is necessary [16]. Biodegradation is the cheapest textile wastewater treatment method. It does not involve any chemicals. The biological processes most often used lead to the detoxification of dyes [17]. The biodegradation of reactive dyes, especially azo dyes, demands a specific sequence of the processes. First, anaerobic conditions must be provided. In strongly reductive conditions double bonds in aromatic amines and polyphenols can be broken [18]. The metabolites of aromatic amines and polyphenols are formed, which are not degraded in the anaerobic process. Those amines may be further mineralized under aerobic conditions [19]. However, the biological processes also have specific limits. They can be used only for the mineralization of biodegradable compounds. The toxic dyes and aromatic amines cannot be biodegraded in biological treatment due to microorganisms, which are sensitive to toxic compounds [20,21]. The removal of aromatic amines from wastewater in textile-dyeing plants occurs through multiple physical, chemical and biological treatment techniques [22]. According to van der Zee and Villaverde [22], the removal rates of aromatic amines in azo dye-containing wastewater generally ranged from 35% to 60% through sequential anaerobic–aerobic reactor systems. However, it is clear that aromatic amines cannot be completely removed from wastewater due to the sorption of aromatic amines to sludge via physical and chemical processes [23]. Twenty-two aromatic amines have been prohibited by Regulation (European Union) 1907/2006, and 24 have been banned in China (GB/T 17592-2011) due to their toxic, carcinogenic and mutagenic characteristics [24].

The textile and dyeing industries discharge high volumes of polluted water including a variety of toxic chemicals [25,26]. One problem is that treated textile wastewater is generally dark red-purple in color, even though the chemical oxygen demand (COD) of the treated textile wastewater may be below the limit for industrial wastewater discharge concentration. Some dyes, polyphenols and aromatic amines and their transformation products are carcinogenic [27,28]. Long-term exposure to carcinogenic chemicals may affect the aquatic river biota and also human health via drinking water [29,30]. Dyes are poorly biodegradable, so inadequately removed in conventional activated sludge plants (10%–20%) with consequent possible significant residual amounts in the discharged effluent. The presence of color in the receiving water body not only causes a negative aesthetic impact, but also can interrupt the photosynthesis, thus negatively affecting the aquatic life [30,31].

Aerobic, anaerobic and sequential anaerobic–aerobic reactors were used for aromatic amine removals [32–34]. Moreover, biological treatment with chemical physical processes such as adsorption on waste sludge and activated carbon, photochemical oxidation and membrane nanofiltration can be used, although the cost is high [34–38].

In recent years, advanced oxidation processes (AOPs) have emerged as potentially powerful methods that are capable of transforming the pollutants into harmless substances [39] and that almost all rely on the generation of very reactive free radicals, such as the hydroxyl radical ($OH^{\bullet}$) [40]. AOPs, generally involving H_2O_2, O_3 or Fenton's reagent as oxidative species for the destruction of contaminants, are alternative techniques for eliminating dyes and other organics in wastewater [41–45]. Semiconductor photocatalysis has emerged as a promising AOP that provides solutions to many environmental pollution problems [41,43–45].

As an important semiconductor material, TiO_2 has been widely used as the photocatalyst because of its chemical and biological inertness, high stability against photocorrosion, non-toxicity, low cost and excellent degradation for organic pollutants [46]. However, practical applications of the TiO_2 are still quite limited, mainly due to the low quantum efficiency and the broad bandgap responding only to UV light [47]. In order to improve the photocatalytic properties of TiO_2, much effort has been made, including transitional metal ion or non-metal element doping [48,49], co-deposition of metals [50] and dye sensitization [51].

Cerium oxide and CeO_2-containing materials have been studied as a good alternative for the oxidation catalysts and supports. It has been shown that when associated with transition metal oxides and noble metals, cerium oxide promotes oxygen storage and releases to enhance oxygen mobility, and forms surface and bulk vacancies to improve the catalyst redox properties of the system [52,53]. Coupling of TiO_2 with CeO_2 attracts much attention because of the special and electron orbital structure and the special properties of CeO_2 [53]. It has been found that the variable valences of Ce such as Ce^{4+} and Ce^{3+} make CeO_2 possess excellent characteristics in transferring electrons and enhancing the light absorption capability in near UV or UV [54]. Meanwhile, doping with CeO_2 can double oxygen reserve and transfer capacity of the TiO_2 photocatalysis [55]. Introducing CeO_2 into the TiO_2 framework could effectively extend the visible light response of TiO_2 [56]. Li et al. [56] have focused on preparing mesostructured CeO_2–TiO_2 with a large surface area and controllable pore size to improve its photocatalytic activity. The large surface area would improve the absorption and mass transfer of target pollutants [57].

Pirkarami et al. [58] found 70% reactive red 19, 75% acid orange 7 (AO7) and 74% acid red 18 removals with 30 mg/L nano-Ni–TiO_2 photocatalyst at pH 7.0 and 25 C. Shao et al. [59] found that 33% methylene blue (MB) dye removal was

obtained with TiO_2–C hybrid aerogel nanocomposite under darkness condition while the MB photodegradation removal was found as 98%, at 500 W UV light, after 150 min at TiO_2/C mass ratio of 0.902, at 25°C [59]. Besson et al. [60] found that 85.2% of 60 mg/L of MB was successfully decolorized under 1.0 g/L of TiO_2 dosage and initial pH 10.5, under sunlight irradiation. Ji et al. [61] reported that with CeO_2 powder and light irradiation, 98% of AO7 was decolorized after 11 h. CeO_2 nanoparticles can able to decolorize the reactive orange 16 dye in the aqueous solution after 2 h [62]. At a reaction temperature of 100°C and an initial pH of 5.0, 98.1% color, 89.6% COD and 65.4% total organic carbon (TOC) reduction were provided with 1 mg/L TiO_2–CeO_2 catalyst [63]. The 10% CeO_2–TiO_2 shows the highest photoactivity under both UV with a degradation rate of 90.3% [64]. Ameen et al. [65] reported that the CeO_2–TiO_2 nanocomposite as photocatalyst accomplished enormously high degradation (70%) of bromophenol dye within 3 h under UV. Li et al. [66] synthesized thermally stable mesoporous ZrO_2–CeO_2–TiO_2 nanocomposite and demonstrated the photodegradation of rhodamine B dye by 90% within 160 min under visible light. The photocatalytic studies performed with real TI ww until now were not concerned with the photoremovals of polyphenols and polyaromatics using CeO_2-doped TiO_2 [67].

The present work focuses on the characterization of CeO_2-doped TiO_2 nanocomposite synthesized under laboratory conditions, with emphasis on the effect of the addition of CeO_2 on the CeO_2-doped TiO_2 photocatalytic activity and on the structural and surface properties of developed nanocomposite. Nitrogen adsorption–desorption and XRD were conducted to characterize the textural and structural properties of the oxides. The surface properties of TiO_2–CeO_2 oxides were investigated by XPS. The CeO_2-doped TiO_2 nanocomposite was first used for the photocatalytic degradation of pollutant parameters (color, polyphenols and polyaromatics) from the TI ww treatment plant in Izmir, Turkey, at different operational conditions such as at increasing photocatalytic times (0, 10, 15, 20, 30, 60, 90 and 120 min), at different CeO_2–TiO_2 mass ratios (1%, 3%, 5%, 10%, 15%, 16%, 25%, 30% and 50%), at different amounts of CeO_2 (1, 3, 5, 8, 10, 15, 20 and 25 mg/L) under 130 W UV irradiation, respectively. Removal efficiencies of color, polyphenols, polyaromatics and their metabolites in TI ww were detected during photocatalytic experiments.

2. Materials and methods

2.1. Raw wastewater

The TI ww used in this study contained color (>230 1/m), total phenol (>200 mg/L), $COD_{dissolved}$ (>770 mg/L) and high biochemical oxygen demand – 5 d (BOD_5) (>251 mg/L) concentrations with a $BOD_5/COD_{dissolved}$ ratio of 0.39. The characterization of TI ww was shown in Table 1 for minimum, medium and maximum values.

2.2. Operational conditions

The effects of increasing irradiation times (0, 10, 15, 20, 30, 60, 90 and 120 min) of increasing CeO_2–TiO_2 mass ratios (1%, 3%, 5%, 10%, 15%, 16%, 25%, 30% and 50%) and of increasing CeO_2-doped TiO_2 nanocomposite concentrations (1, 3, 5, 8, 10, 15, 20 and 25 mg/L) on the photoremovals of polyphenols and total aromatic amines were investigated. Color, polyphenols

Table 1
Characterization of TI ww (n = 3, mean values ± SD)

Parameters	Values		
	Minimum	Medium	Maximum
pH	5.10 ± 0.18	5.65 ± 0.20	6.20 ± 0.22
DO (mg/L)	1.32 ± 0.05	1.43 ± 0.05	1.54 ± 0.05
ORP (mV)	86.00 ± 3.01	107.55 ± 3.76	129.10 ± 4.52
TSS (mg/L)	286.00 ± 10.01	360 ± 12.6	434.00 ± 15.20
TVSS (mg/L)	193.00 ± 6.8	242.10 ± 8.47	291.20 ± 10.2
COD_{total} (mg/L)	932.60 ± 32.62	1,171.40 ± 41.00	1,410.10 ± 49.40
$COD_{dissolved}$ (mg/L)	771.30 ± 27.00	968.8 ± 33.91	1,166.30 ± 40.82
TOC (mg/L)	463.30 ± 16.22	582.90 ± 20.40	702.40 ± 24.60
BOD_5 (mg/L)	252.60 ± 8.84	315.4 ± 11.04	378.20 ± 13.24
$BOD_5/COD_{dissolved}$	0.37 ± 0.02	0.39 ± 0.014	0.41 ± 0.02
Total N (mg/L)	25.70 ± 0.90	30.96 ± 1.08	36.22 ± 1.27
NH_4–N (mg/L)	1.87 ± 0.07	2.25 ± 0.08	2.63 ± 0.092
NO_3–N (mg/L)	8.10 ± 0.28	10.2 ± 0.36	12.20 ± 0.43
NO_2–N (mg/L)	0.14 ± 0.005	0.16 ± 0.006	0.18 ± 0.006
Total P (mg/L)	8.90 ± 0.31	11.05 ± 0.39	13.20 ± 0.46
PO_4–P (mg/L)	6.34 ± 0.22	8.03 ± 0.28	9.72 ± 0.34
SO_4^{2-} (mg/L)	1,250.10 ± 43.80	1,560.8 ± 54.63	1,871.40 ± 65.50
Color (m^{-1})	72.81 ± 2.62	400.07 ± 3.25	507.20 ± 3.80
Total phenol (mg/L)	234 ± 8.2	220 ± 16.4	702 ± 24.6
TAAs (mg benzidine/L)	310 ± 10.9	420 ± 21.7	930 ± 32.6

(quercetin, fisetin, ellagic acid, carminic acid, luteolin and curcumin) and polyaromatics (2,6-dimethylaniline [2,6-DMA], 2-aminoanisole [MOA], 2,4-toluenediamine [TDA], 2-naphthylamine [NA], 4,40-thiobisbenzenamine [TOA], 3,3-dichlorobenzidine [DCB] and 3,30-dimethoxybenzidine) removal efficiencies were observed during photocatalytic experiments at constant 130 W UV power, at original TI ww pH of 6.2 and at a temperature of 21°C.

2.3. Analytical methods

pH, *T* (°C), oxidation-reduction potential (ORP) (mV), TSS, TVSS, DO, BOD_5, COD_{total}, $COD_{dissolved}$ and TOC were monitored following Standard Methods 2550, 2580, 2540 C, 2540 E, 5210 B, 5220 D, 5310 and 5520 B, respectively [68]. Total nitrogen, NH_4–N, NO_3–N, NO_2–N, total phosphorous, PO_4–P, total phenol and SO_4^{2-} were measured with cell test spectroquant kits (Merck, Germany) on a spectroquant NOVA 60 (Merck, Germany) spectrophotometer (2003). The total phenol was monitored as follows: 40 mL of TI ww was acidified to pH = 2.0 by the addition of concentrated HCl. Phenols were then extracted with ethyl acetate. The gas chromatography-mass spectrometry-mass spectrometry (GC-MS-MS) (Hewlett-Packard 6980/HP5973MSD) was used for the identification and quantification of polyaromatics, polypehols and their metabolites. Tables 2(a) and (b) present the retention times, exact masses of the molecular ions (m/z), mass fragments (ESI), and proposed molecular structures of polyphenols and their metabolites and molecular structures of aromatic amines and their metabolites, respectively.

2.4. Preparation of CeO_2-doped TiO_2 nanocomposite under laboratory conditions

In the synthesis of CeO_2-doped TiO_2 nanocomposite the procedure given by Liu et al. [64] was partially modified: 0.005 mol of 1-hexadecane-3-methylimidazolium bromide ($C_{16}MIM^+Br^-$) was dissolved in 15 mL of distilled water with vigorous stirring at 40°C for 30 min. Then certain amounts of tetrabutyl orthotitanate and $Ce(NO_3)_3$ (total amount of Ti plus Ce was 0.0015 mol) were added into the above solution. The molar proportion of Ce in the composition was varied in the range of 1%, 3%, 5%, 10%, 15%, 16%, 25%, 30% and 50%. After stirring for 30 min, pH value was adjusted to 9–10 by dropwise addition of ammonia solution. After stirring for another 2 h, the mixture was transferred to a 100-mL Teflon-lined stainless steel autoclave at 100°C for 2 d. Then the product was recovered by filtration, washed thoroughly with deionized water,

Table 2(a)
Identification of polyphenols and their metabolites in TI ww (15 mg/L CeO_2-doped TiO_2 with a CeO_2 ratio of 15 wt%, pH = 6.2, after 10 min photooxidation time and at 21°C at a UV power of 130 W)

Polyphenols and their metabolites					
RT (min)	UV (λ_{max}) (nm)	$[M–H]^-$ (*m/z*)	MS fragments (ESI)	Identification	Molecular structure
29	343	464.2	412.1	Quercetin (QUC)	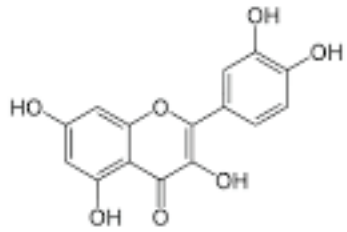
3.29	303	385	408.1	Isorhamnetin (ISO)	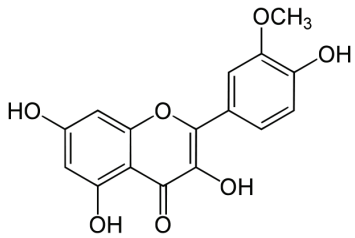
4.67	300	303	209.4	Tamarixetin (TMR)	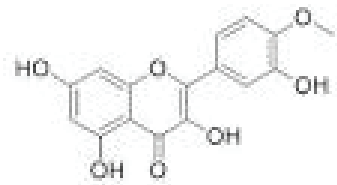

(*Continued*)

Table 2(a) (*Continued*)

Polyphenols and their metabolites					
RT (min)	UV (λ_{max}) (nm)	$[M–H]^-$ (*m*/*z*)	MS fragments (ESI)	Identification	Molecular structure
5.89	302	297	219.1	Curcumin (CUR)	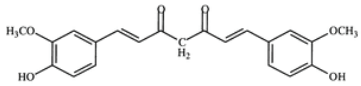
23	313	691.7	598.08	Bisdemethoxycurcumin (BDG)	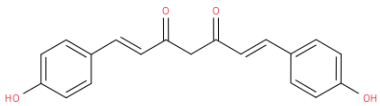
18	298	234.4	212.3	*O*-Glucuronide (*O*-GLC)	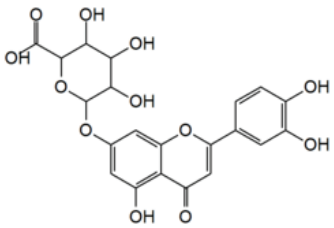
19	296	198.2	176.9	Curcumin *O*-sulfate (COS)	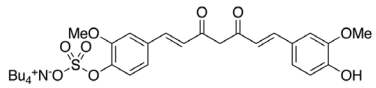
15	323	349	312.09	Carminic acid (CMA)	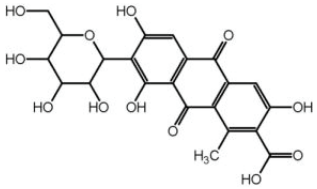
14	310	305.06	300.7	*C*-Glucoflavokermesic (*C*-GFK)	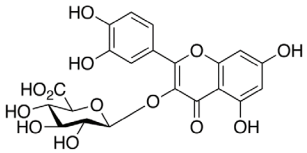
16	312	312.09	310	*C*-Glucopyranosyl flavokermesic acid (GPDA)	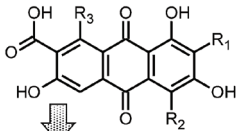
15	310	398.07	389	2-(3,4-Dihydroxyphenyl)-5,7-dihydroxy-4-chromenone (LUTEOLIN)	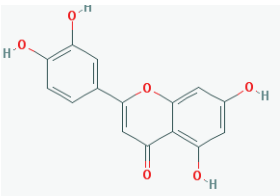
14	299	234.45	289	3′-Methyl luteolin (3-MLN)	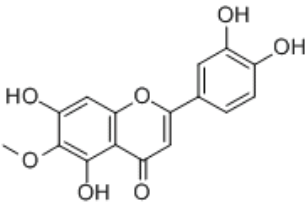

(*Continued*)

Table 2(a) (*Continued*)

Polyphenols and their metabolites					
RT (min)	UV (λ_{max}) (nm)	$[M–H]^-$ (*m*/*z*)	MS fragments (ESI)	Identification	Molecular structure
12	278	205.09	279	*O*-Glucuronide (*O*-GLC)	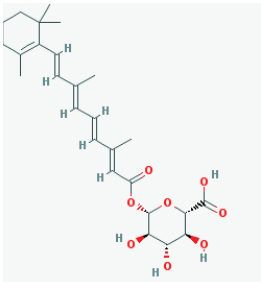
24.3	301	198.13	197.12	3,7,3′,4′-Tetrahydroxyflavone (FISETIN)	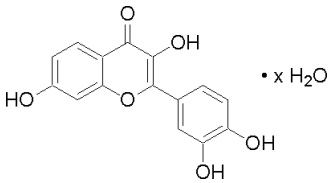
15	276	123.98	111	3-4-Catechol (3-4-CATECH)	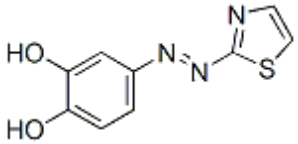
12	254	104.12	56	2,3,7,8-Tetrahydroxy-chromeno[5,4,3-cde]chromene-5,10-dione (ELLAGIC ACID)	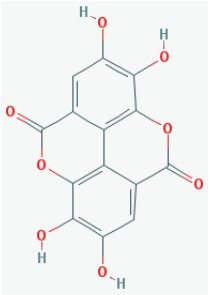
12	560	289	180	3,8-Dihydroxy-6H-dibenzopyran-6-one (3,8-DHBP)	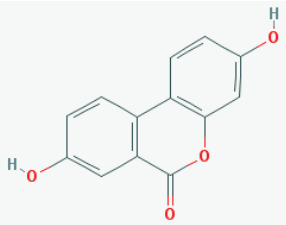
32	450	290	110		
18	450	340	190	3-Hydroxy urolithin (3-HUL)	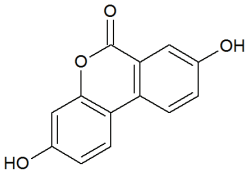
18	380	180	89		
21	650	340	120	7-Hydroxy-3,4-benzocoumarin (7-HBC)	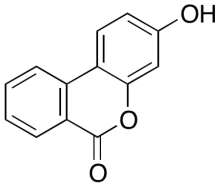
15	290	160	90		

Table 2(b)
Identification of polyaromatic amines and their metabolites in TI ww (15 mg/L CeO_2-doped TiO_2 with a CeO_2 ratio of 15 wt%, pH = 6.2, after 10 min photooxidation time and at 21°C at a UV power of 130 W)

Polyaromatic amines and their metabolites					
RT (min)	UV (λ_{max}) (nm)	$[M–H]^-$ (m/z)	MS fragments (ESI)	Identification	Molecular structure
18	323	458	340	3,5-Aminoanisole (3,5-MOA)	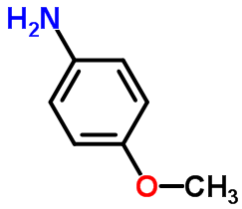
				3,5-*cis*-l,2-Dihydroxy-3-methoxycyclohexa-3,5-diene (3,5-*cis*-1,2 HMCH)	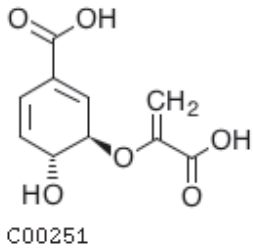 C00251
20	309	216	209	2-Methoxyphenol (2-MOPH)	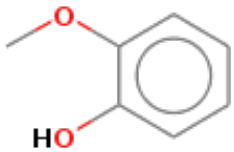
25	323	483.2	406	Benzene-1,2-diol (CATECHOL)	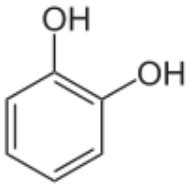
15	305	123.4	112.8	Phenol (PHE)	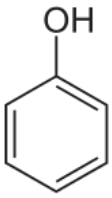
18	302	116.5	110.3	2,4-Toluenediamine (TDA)	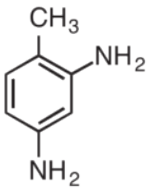
18.9	324	213.8	210	4-Acetylamino-2-aminotoluene (4-ACETOL)	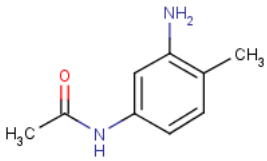

(*Continued*)

Table 2(b) (*Continued*)

Polyaromatic amines and their metabolites					
RT (min)	UV (λ_{max}) (nm)	$[M–H]^-$ (*m*/*z*)	MS fragments (ESI)	Identification	Molecular structure
15	320	189.6	170	2,4-Diacetylaminotoluene (2,4-DIACETAOL)	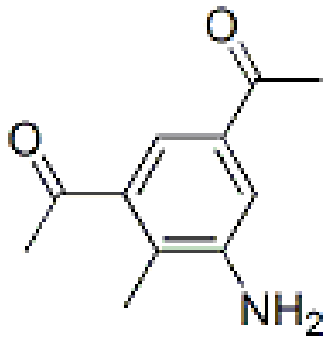
12	307	165.9	160	4-Acetylamino-2-aminobenzoic acid (4-ACEATOBA)	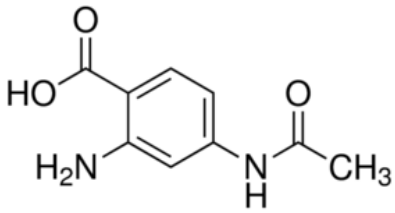
27	342	595.1	88	2,4-Diacetylaminobenzoic acid (2,4-DIACETOBA)	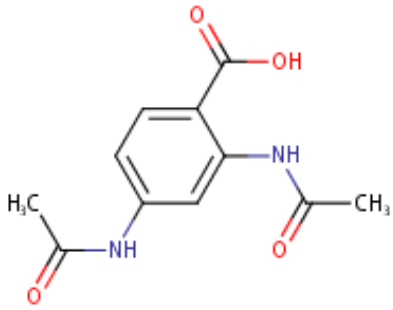
21	301	234.98	143	2,6-Dimethylaniline (2,6-DMA)	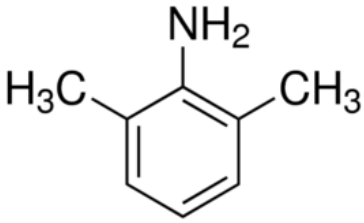
19	298	222	231	4-Hydroxy-2,6-dimethylaniline (4-HDA)	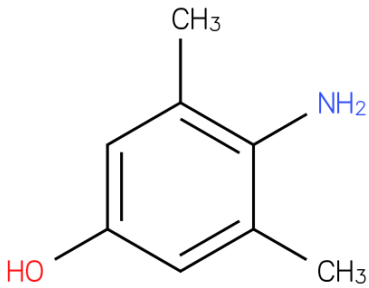

(*Continued*)

Table 2(b) (*Continued*)

Polyaromatic amines and their metabolites					
RT (min)	UV (λ_{max}) (nm)	$[M–H]^-$ (*m*/*z*)	MS fragments (ESI)	Identification	Molecular structure
16	239	201.87	169	2-Amino-3-methylbenzoic acid (2-A-3-MBA)	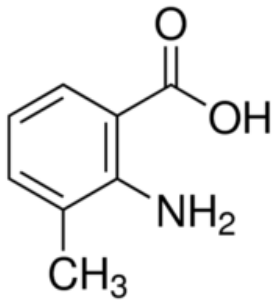
17	235	198.	124	2,6-Dimethylnitrosobenzene (2,6-DMNB)	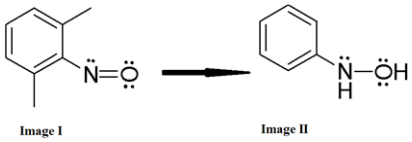
24	343	459.45	232	3,3′-Dichlorobenzidine (3,3-DCB)	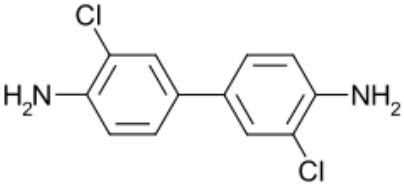
13	278	201	97	*N*-Acetyl 3,3′-dichlorobenzidine (N-AC DBC)	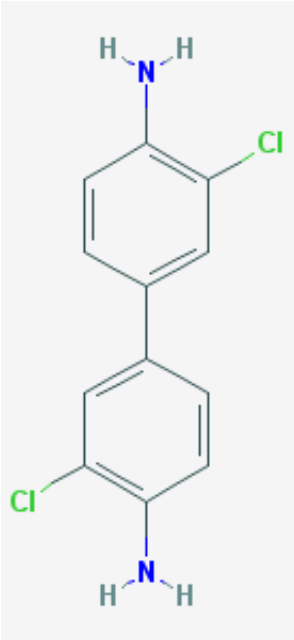
9	260	202	198	3,3′-Dichlorobenzidine (N,N-DAC DBC)	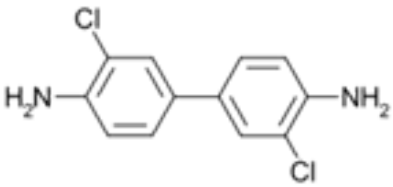

and dried at 100°C overnight. The synthesized material was calcined in air at 550°C for 2 h to remove the template.

2.5. Characterizations methods of CeO_2-doped TiO_2 nanocomposite

The morphological observations (shape and size of the nanocomposite) were observed by field-emission scanning electron microscope (FESEM; Hitachi S-3400). X-ray powder diffraction (XRD) patterns for the samples were collected at a scan rate of 1/min in the 2θ range of 20°–65° using a Scintag-I XRD instrument equipped with Cu Kα radiation [69,70]. The working voltage of the instrument was 35 kV, and the current was 35 mA [71,72]. The mean crystallite size of samples was calculated from peak broadening by the Scherrer equation using Jade 6.5 software, where the Scherrer constant *K* (particle shape factor) was taken as 0.85 as reported by Muñoz-Batista et al. [70]. Nitrogen adsorption–desorption isotherms were obtained using a nitrogen adsorption apparatus (ASAP 2020, USA) [73]. All the samples were degassed at 200°C prior to measurements. The Brunauer–Emmett–Teller (BET) surface area and pore size distribution of CeO_2 and TiO_2 were obtained from eight-point nitrogen adsorption/desorption analysis with a Quantachrome Autosorb-1 [73]. All samples were outgassed at 220°C prior to the adsorption–desorption measurements. Micropore surface area and volume were calculated using the *t*-method [71]. The pore size distribution was calculated by applying the Barrett–Joyner–Halenda (BJH) method on the desorption branch of the isotherm curve [71]. The UV Raman spectra were obtained on a UV–high spectral resolution Raman spectrograph, using the He–Gd laser of 325 nm as the excitation wavelength [70,72]. The spectra acquisition consisted of two accumulations of 60 s for each sample, and the spectral resolution was 4 cm^{-1}. A spectra range of 30–700 cm^{-1} was obtained. Energy-dispersive spectroscopy (EDS; Oxford INCA) was utilized to have an analysis of the chemical composition of the products. X-ray photoelectron spectroscopy (XPS) spectra were recorded on a Kratos Analytical Axis Ultra spectrometer with monochromatic aluminum. The X-ray source was operated at 14 kV and 20 mA. The sample powders were pressed into 5 mm × 5 mm 3 M double-sided tape using a mortar and pestle, and visualized by a stereomicroscope to ensure complete coverage and powder uniformity over the tape [74]. Prior to the analysis, oxide samples were dried overnight in an oven at 120°C under atmospheric pressure. After drying, all samples were immediately stored in a container and mounted for analysis [74]. Sample height positions were set from O 1s signal at 529 eV following changing of lateral coordinates so that the measured signal from the sample powders were maximized, thus minimizing any possible signal from the 3 M double-sided tape [74]. The 3 M tape was examined independently, and the characteristic shape of the C 1s line was not found when compared with the C 1s line collected from these sample powders. As a reference, C 1s signal of the adventitious carbon in which it was fixed at 285 eV was used. A survey scan with analyzer pass energy of 80 eV was initially recorded for the sample to identify elements present. The composition and chemical states were determined from the charge-corrected high-resolution scans with an analyzer pass energy of 20 eV. To better understand the influence of cerium, photoluminescence (PL) emission spectroscopy was studied not only to confirm the presence of surface defects [69,74]. Hence, PL spectra were plotted in the range of 360–700 nm using an excitation source around 330 nm.

All experiments were carried out three times, and the results given as the means of triplicate samplings. Individual TI ww concentrations were given as the mean with standard deviation (SD) values.

3. Results and discussion

3.1. FESEM analysis results

The morphology of the prepared CeO_2-doped TiO_2 nanocatalyst was studied using FESEM, and the images are shown in Fig. 1. Highly aggregated more or less spherical-shaped particles were observed for the TiO_2 sample (Fig. 1(a)). Quite big flake-like morphology was observed for the CeO_2 (Fig. 1(b)). The CeO_2-doped TiO_2 sample represented a porous structure (Fig. 1(c)), and they were homogeneously mixed together.

3.2. XRD analysis results

Fig. 2 shows the XRD patterns of the CeO_2-doped TiO_2 nanocomposite. The peak locations and relative intensities are cited from the Joint Committee on Powder Diffraction Standards (JCPDS) database. The sharp diffraction peaks at 2θ values of 25°, 37°, 47°, 54° and 62° are indexed to the (101), (004), (200), (105) and (204) planes of the anatase phase of TiO_2 (JCPDS No. 21-1272), and the peaks at the 2θ of 27° and 36° are fitted well with the (110) and (101) planes of rutile phase of TiO_2 (JCPDS No. 21-1276). It shows that the TiO_2 exists in both anatase and rutile phases. The diffraction peaks of 2θ at 25.3°, 37.8°, 40.8°, 53.9°, 55.1°, 62.7° and 75.1° are assigned to the (101), (004), (200), (105), (211), (204) and (219) planes of TiO_2, respectively, as reported by Wang et al. [69] and Muñoz-Batista et al. [70]. The diffraction peaks at the 2q values of 32°C, 47°C and 57°C are also shown in Fig. 2. These indicates the cubic-fluorite crystalline structure of ceria without any other impure phases (JCPDS No. 01-078-0694) fitted well with the (200), (220) and (311) planes. In the CeO_2-doped TiO_2, both anatase and rutile phases of titania were noticed. It indicates the fine dispersion of ceria on TiO_2 without further phase segregation. Moreover, it partly inhibited the growth of rutile phase of TiO_2 crystallite. The sharp diffraction peaks at 2q values of 26°C, 36°C, 46°C and 53°C are indexed to the (101), (004), (220) and (211) planes of the CeO_2-doped TiO_2 nanocomposite. This agrees with previous researches performed by Karunakaran and Gomathisankar [71] and Santiago-Morales et al. [72].

3.3. Nitrogen adsorption/desorption isotherm results

Fig. 3 shows the nitrogen adsorption/desorption isotherms of CeO_2-doped TiO_2 nanocomposite. Both isotherms are similar to type IV according to International Union of Pure and Applied Chemistry classification, indicating the mesoporous texture of the samples as reported by Ghasemi et al. [73].

3.4. BET analysis results

The BET surface area, pore volume and the average pore for both samples are listed in Table 3. The BET surface area

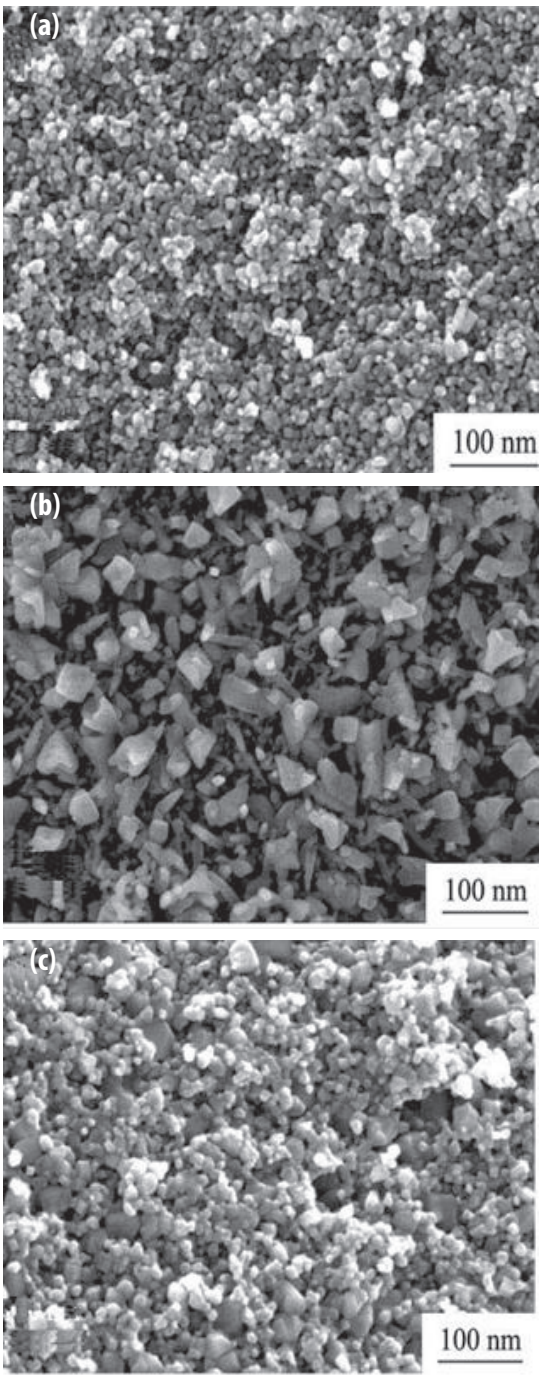

Fig. 1. FESEM analysis of TiO_2 sample (a); CeO_2 sample (b) and CeO_2-doped TiO_2 nanocomposite sample (c).

of CeO_2–TiO_2 catalyst is higher than that of bare TiO_2. These results are in agreement with the XRD analysis results. The particle size of TiO_2, CeO_2 and 15 mg/L CeO_2-doped TiO_2 nanocomposite with a CeO_2 ratio of 15% were 198.4, 86.2 and 265 nm, respectively, which were calculated by the Scherrer equation (Table 3). As the CeO_2 ratios in CeO_2-doped TiO_2 nanocomposite were increased from 1% to 3%, 5%, 10% and 15% the surface area, pore volume and average pore size increased. Further increasing the CeO_2 ratio to 25% and 50%

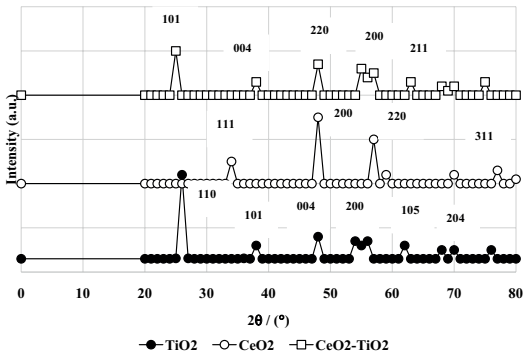

Fig. 2. XRD patterns of TiO_2-, CeO_2- and CeO_2-doped TiO_2 nanocomposites.

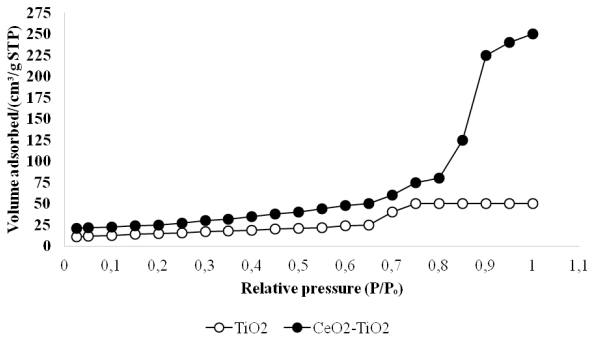

Fig. 3. N_2 adsorption/desorption isotherms of TiO_2 and CeO_2 in CeO_2-doped TiO_2 nanocomposite.

Table 3
Surface area, pore volume and average pore size properties of CeO_2-, TiO_2- and CeO_2-doped TiO_2

Nanomaterials	Surface area (m^2/g)	Pore volume (cm^3/g)	Average pore size (A)
TiO_2	198.4	0.169	33
CeO_2	86.2	0.052	17
CeO_2–TiO_2 (1%)	148.5	0.178	35
CeO_2–TiO_2 (3%)	168.2	0.189	53
CeO_2–TiO_2 (5%)	183.9	0.278	56
CeO_2–TiO_2 (10%)	220.2	0.293	66
CeO_2–TiO_2 (15%)	265.2	0.560	82
CeO_2–TiO_2 (25%)	265	0.560	82
CeO_2–TiO_2 (50%)	265	0.560	82
	Types		
Commercial CeO_2	2.1	0.022	38
TiO_2	12.8	0.132	19

for the aforementioned parameters of the surface area, pore volume and average pore size remained the same. The single oxides exhibited significantly higher surface areas than those of corresponding commercial CeO_2 and TiO_2. Mixing TiO_2 and CeO_2 in the synthesis stage led to a synergetic increase of surface area.

3.5. Raman spectral analysis

The Raman spectra of CeO_2-doped TiO_2 nanocomposite showed the characteristic signals for the tetragonal phase of TiO_2 (anatase) around 156, 410, 547 and 670 cm^{-1} as reported by Santiago-Morales et al. [72] (Fig. 4). The CeO_2 fluorite type phase was detected in the spectrum of the CeO_2/TiO_2 nanocomposite. The band at 460 cm^{-1} corresponded to the cubic phase of the CeO_2 fluorite-type phase. Moreover, the band at 595 cm^{-1} was attributed to the oxygen vacancies in the CeO_2 lattice as reported by Santiago-Morales et al. [72] and Muñoz-Batista et al. [70] (Fig. 4).

3.6. EDS analysis

The EDS spectrum of CeO_2/TiO_2 nanocomposite is shown in Fig. 5. Ti, Ce, O elements were detected with the absence of other elements, suggesting Ce in the form of CeO_2 had been successfully mixed with TiO_2.

3.7. XPS analysis results

XPS analysis was conducted to understand the surface chemical state of Ce and Ti in CeO_2-doped TiO_2 nanocomposite. The Ti 2p core level spectrum of TiO_2 arrays and CeO_2-doped TiO_2 arrays are illustrated in Fig. 6(a). The binding energy at 458.7 and 464.4 eV was attributed to Ti $2p_{3/2}$ and Ti $2p_{1/2}$, respectively, in the TiO_2 arrays as reported by Contreras-Garciaa et al. [74]. Compared with TiO_2 arrays, the binding energy of CeO_2-doped TiO_2 nanocomposite arrays increased slightly. This could be due to the different electronic interaction between titanium and cerium, which indicated that Ti^{3+} species were formed in the CeO_2-doped TiO_2 nanocomposite arrays [75]. Six XPS peaks were found to be as the characteristic peaks of Ce^4, Ce 3d (Fig. 6(b)). v and u indicated the spin-orbit coupling $3d_{5/2}$ and $3d_{3/2}$ respectively. The peaks of v and u were assigned to Ce(IV) ($3d^94f^2$) O ($2p^4$) state; the peaks of v_2 and u_2 were assigned to Ce(IV) ($3d^94^{fl}$) O ($2p^5$) state; and

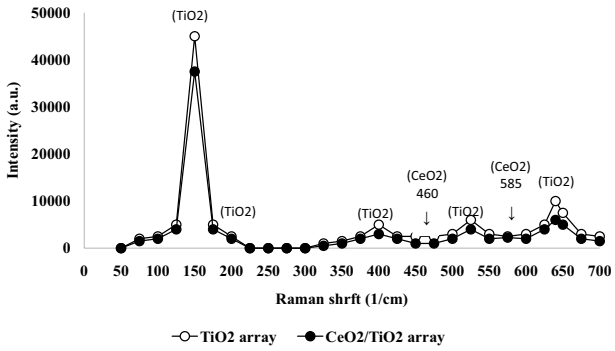

Fig. 4. Raman spectra of TiO_2- and CeO_2-doped TiO_2 nanocomposite.

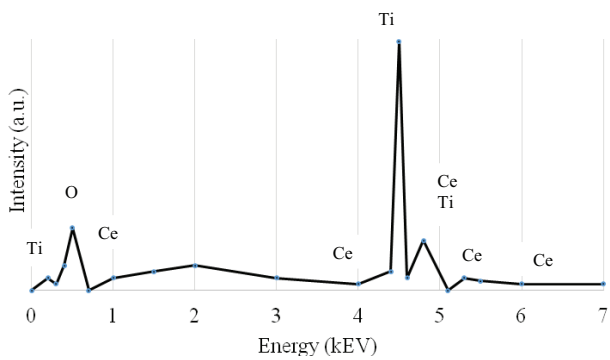

Fig. 5. EDS spectrum of CeO_2-doped TiO_2 nanocomposite.

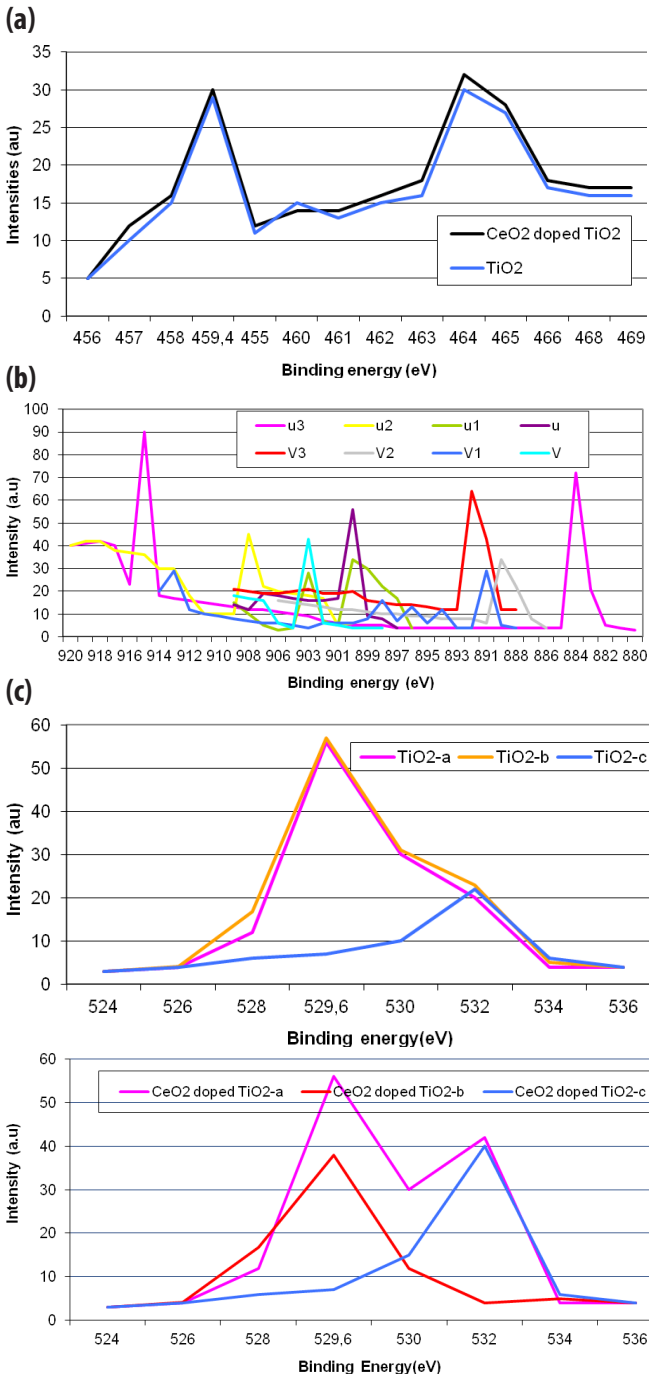

Fig. 6. Ti 2p (a) Ce 3d (b) and O 1s (c) core level spectra collected for TiO_2 and CeO_2-doped TiO_2 nanocomposite in XPS analysis.

the peaks of v_3 and u_3 were assigned to Ce(IV) ($3d^9 4f^0$) O ($2p^6$) state. The peaks labeled as v_1 and u_1 were attributed to Ce(III) ($3d^9 4f^2$) O ($2p^5$) state. Therefore, a mixture of Ce^{3+}/Ce^{4+} oxidation states existed on the surface of the sample as reported by Liu et al. [64]. Fig. 6(c) shows that the O 1s core level was composed of at least two components. The O 1s signal at about 529.6 eV was assigned to the lattice oxygen (O^{2-}) for TiO_2 and CeO_2 according to the literature, while the signal at 532.0 eV was probably due to the oxygen in surface hydroxyl groups as reported by Qian et al. [76] and Fang et al. [77]. The signal at 532.0 eV can be associated to surface hydroxyl groups [76–78]. The existence of this peak was due to defects in the subsurface. An optimum concentration of Ce^{3+} and more oxygen vacancies may promote photocatalysis activity. It can be noticed that the introduction of CeO_2 species can effectively enhance the surface hydroxyl groups on the surface of the mesoporous TiO_2. In this study it was found that the highest surface concentration of hydroxyls appeared to be CeO_2-doped TiO_2 with a mass ratio of 15% according to the studies performed [75].

3.8. PL analysis results

The PL spectra were plotted in the range of 360–700 nm using an excitation source around 300 nm to determine the influence of cerium, PL emission spectroscopy throughout surface defects (Fig. 7). Five different main patterns were observed in the PL spectra: a UV emission peak at 380 nm was obtained due to phonon-assisted indirect transition from the edge (*X*) to the center (*T*) of the Brillouin zone as reported by Yu et al. [79]. The emission peak at 429 nm was related to self-trapped electrons recombining with holes inside the bulk lattice of TiO_2 [74]. Emission peaks at 457 and 535 nm were related to the surface oxygen defect sites as mentioned by Contreras-Garcíaa et al. [74] and Wang et al. [69]. The emission peak at 491 nm was due to charge transfer from Ti^{3+} to TiO_6^{2-} octahedral [69].

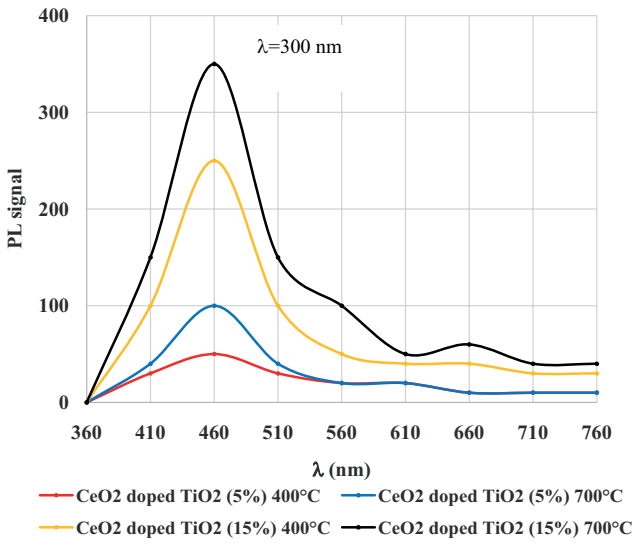

Fig. 7. PL signal of CeO_2-doped TiO_2 nanocomposite with 5 and 15 wt% CeO_2-doped TiO_2 nanocomposite calcined at 400°C and 700°C.

A much higher PL intensity was found for 15 wt% CeO_2-doped TiO_2 at 400°C compared with CeO_2-doped TiO_2 with 5% CeO_2. This higher intensity was mainly due to a prominent peak at 457 nm showing that Ce increased the number of surface oxygen defects. This could be related to the higher radius of Ce^{4+} (0.93 Å) than that of Ti^{4+} (0.605 Å) inducing a distortion of the TiO_6 octahedra during the incorporation of Ce and generating surface oxygen vacancies to maintain charge neutrality as reported by Contreras-Garciaa et al. [74].

Calcination at 700°C led to an important increase of the PL intensity for 15% CeO_2-doped TiO_2, and it was characterized by a dominant peak at 457 nm; some contributions at 429 and 491 nm. This shows that calcining at 700°C not only induces the creation of surface defect sites but also strongly increases the bulk recombination rate inside the TiO_2 lattice. Although the addition of CeO_2 to TiO_2 with a ratio of 15% at 700°C quenches the PL signal, there was still a discernible contribution from surface oxygen vacancies. A lower number of surface oxygen vacancies would be formed with the increase of the calcination temperature at 15% CeO_2 containing 15 mg/L CeO_2-doped TiO_2.

PL results show that the role of cerium is mainly to generate surface oxygen vacancies able to trap photogenerated electrons and leaving photogenerated holes available for oxidation reactions. Cerium also limits the bulk recombination rate by restricting the anatase crystallite growth. This restriction is related to the creation of surface defects limiting the bulk recombination rate.

3.9. Effect of the amount of CeO_2 ratio in CeO_2-doped TiO_2 nanocomposite for the photodegradation of total polyaromatic amines and polyphenols

The photodegradation of total polyaromatic amines and polyphenols increased from 50% and 55% up to 90% and 88%, respectively, by increasing the amount of CeO_2 content from 1% to 10% in the 15 mg/L CeO_2-doped TiO_2 nanocomposite and reaches maximum (98% and 97% for total polyphenols and total polyaromatics, respectively) at 15% after 30 min irradiation time at a UV power 130 W (Figs. 8(a) and (b)). Further increasing the CeO_2 content to 20%, 30% and 50% in the 15 mg/L CeO_2-doped TiO_2 concentration led to decreases in photodegradation of the pollutants (to around 90% and 80%). The enhancement of the photocatalytic activity for degradation could be attributed to the excellent electric conductivity and large specific surface area of CeO_2-doped TiO_2 nanocomposite. The photogenerated electrons are transported to the surface of the nanocomposites more easily; thus, the recombination between photoinduced electrons and holes was inhibited [3]. Decrease of the photocatalytic activity with higher CeO_2 content may be due to the fact that the opportunity for the collision of electrons and holes increases; therefore, the recombination of the photogenerated electron–hole pairs is promoted. Increasing the CeO_2 ratio in the CeO_2-doped TiO_2 nanocomposite ratio also lowered the contact surface of TiO_2 nanoparticles with the illuminated light [4]. With an optimum CeO_2 ratio in the 15 mg/L CeO_2-doped TiO_2 nanocomposite the maximum photodegradation yields were observed for polyphenols and polyaromatics.

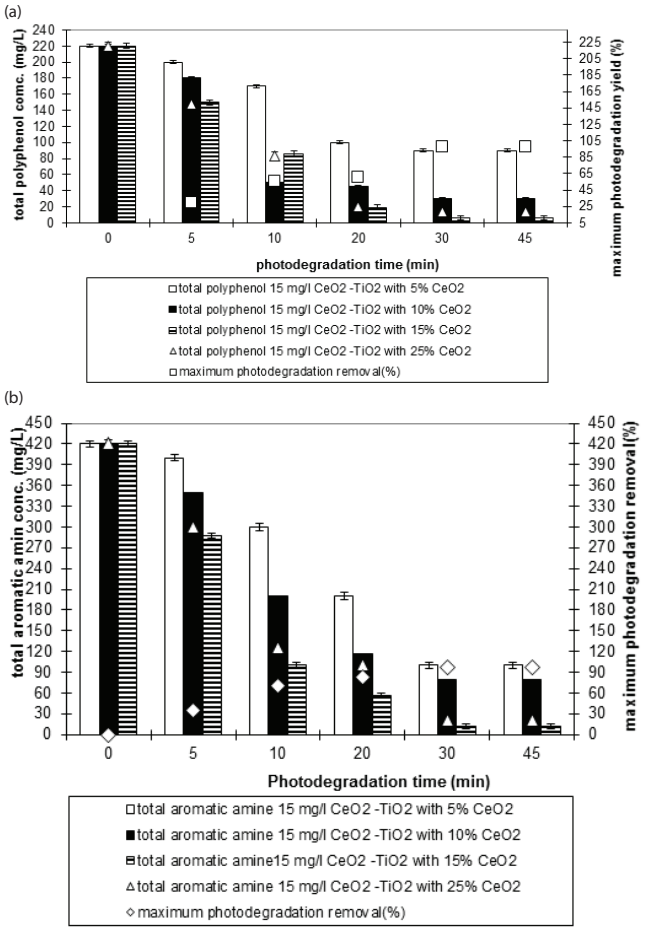

Fig. 8. (a) Photodegradation of total polyphenol at increasing of CeO_2 ratios in 15 mg/L CeO_2-doped TiO_2 nanocomposite vs. photodegradation time at an UV power of 130 W and at pH = 6.2 and at a temperature of 21°C. (b) Photodegradation of total aromatic amines at increasing of CeO_2 ratios in 15 mg/L CeO_2-doped TiO_2 nanocomposite vs. photodegradation time at an UV power of 130 W at a pH = 6. 2 and at a temperature of 21°C.

3.10. Effects of bare CeO_2, TiO_2 and CeO_2-doped TiO_2 nanocomposite concentrations on the photodegradation yields of color under 130 W UV power

The photocatalytic degradation rate of color with 5, 15, 25 and 50 mg/L pure CeO_2, pure TiO_2 and CeO_2-doped TiO_2 nanocomposite concentration with a CeO_2 ratio of 15% were studied under 30 min with 130 W UV irradiation. As the CeO_2-doped TiO_2 concentration was increased from 5 to 15 mg/L, the color yields increased from 74% up to 96% (Fig. 9). Further increase of CeO_2-doped TiO_2 nanocomposite did not significantly affect the color yield. The color yields at 25 and 50 mg/L remained as is in 15 mg/L CeO_2-doped TiO_2 nanocomposite level. Fig. 9 also demonstrates that the pure TiO_2 and pure CeO_2 exhibited lower color photodegradation rates (54% and 48%, respectively) than that CeO_2-doped TiO_2 nanocomposite since the bare nanocatalysts could not be effectively activated by visible lights due to big energy bandgaps of bare TiO_2 compared with CeO_2 (3.18 eV for TiO_2

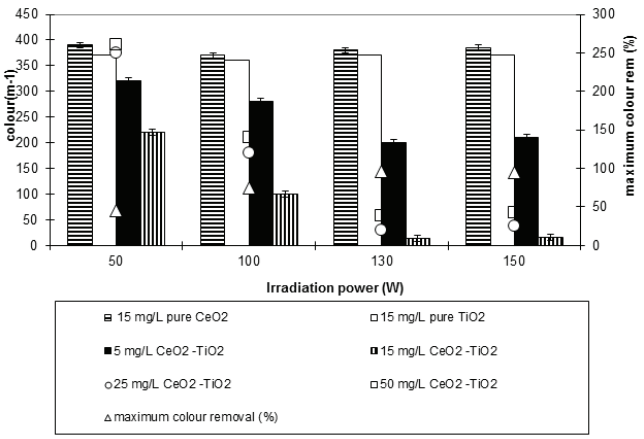

Fig. 9. Effects of CeO_2 mass ratios in the CeO_2-doped TiO_2 nanocomposite to photocatalytic removals of color in TI ww under 130 W UV irradiation at original TI ww pH of 6.2 at a temperature of 21 C after 30 min irradiation.

and 2.88 eV for CeO_2) as reported by Liu et al. [64] (data not shown). Modification of TiO_2 with CeO_2 resulted in abrupt increase of the color photodegradation efficiency owing to the CeO_2-doped TiO_2 photosensitization as reported by Liu et al. [64]. This fact is consistent with its smaller particle size, larger surface area, optimum concentration of Ce^{3+} and highest concentration of surface hydroxyl (OH•) groups. This can also be attributed to the fact that when doping content of CeO_2 is an optimum amount, the CeO_2 particles well dispersed on the TiO_2 surface can act as electron–hole separation centers. When the doping of the CeO_2 concentration exceeds a certain amount (≥15%), the trap center may become the recombination center of photogenerated electrons and holes. Meanwhile, the excessive cerias result in agglomeration of CeO_2 nanoparticles, which will scatter the incident light, lowering the photoquantum efficiency of the photocatalytic reaction as reported by Liu et al. [64]. After 30 min irradiation time the color yield remained constant or decreased slightly at all CeO_2 to TiO_2 mass ratios.

The majority of color was degraded within the first 28 min. Thus, the synthesized CeO_2–TiO_2 nanocomposite could be a good visible-light driven photocatalyst for the degradation of color originating from the dyes in the TI ww as catalyst under light illumination. The mechanism of color photodegradation can be summarized as follows: Upon 130 W light illumination, CeO_2 firstly absorbs light, and the photoexcited electron moves to the conduction band (CB) of CeO_2 where the CB level is higher than the CB level of TiO_2 nanoparticles. The photoexcited electrons inject into CB of TiO_2, which easily scavenges the electrons to produce the large amount of reactive holes. The existence of the mixture of Ce^{3+}/Ce^{4+} oxidation states on the surface of nano-CeO_2–TiO_2, denotes the fact that the nanocomposite is not fully oxidized, so that Ce^{4+} can easily capture electrons and prevent the combination of photogenerated electrons and holes, resulting in a higher quantum efficiency of photocatalytic reaction [3]. Secondly, the photoinduced electrons in the TiO_2 can drift to the CeO_2 under the inner electric field between CeO_2 and TiO_2 due to the energy band bending in space charge region. It is more helpful for the separation of

photoinduced electron–hole pairs in TiO_2, resulting in the improvement of photocatalysis under UV illumination [67]. In addition, with the doping of CeO_2, the abundant surface hydroxyl groups exist on the surface of TiO_2, which can be attacked by photoinduced holes and yield surface $OH^{\bullet}$ radicals with high oxidation capability [64].

3.11. Polyphenols and their metabolites in TI ww

The dyes in the textile industry are the main source of the color. The dyes used to color textiles are flavonoid compounds: carotenoids, hydroxyketones, anthraquinones, naphthoquinones, flavones, flavonols, flavonones and indigoids, and related compounds. Among these polyphenols, quercetin, fisetin, ellagic acid, carminic acid, luteolin and curcumin concentrations were monitored as color polyphenols in TI ww. The polyphenols transformed by photodegradation of polyphenols by ring cleavage, decarboxylation and dehydroxylation reactions under UV. By hydroxylation of one –OH group in carminic acid two metabolites namely c-glucopyranosyl flavokermesic acid (c-GFK) and glucopyranosyl-dioxoanthracene (GPDA) were produced under UV. In this study, the levels of these metabolites were measured as 25 and 19 mg/L after 10 min photodegradation while the level of the main polyphenol carminic acid was reduced from an initial 64–48 mg/L after 30 min UV irradiation (Fig. 10(a)). The carminic acid and metabolite concentrations were reduced to 1 mg/L, 1.2 and 1.8 mg/L with metabolte yields of 98 and 99%, respectively. Although carminic acid showed negative genotoxicity in a somatic mutation and recombination test of Drosophila melanogaster, hydroxylated forms of carminic acid were found to be slightly toxic [80,81]. Jørgensen and Skibsted [82] found that the photolability of carminic acid increased with deprotonation and was

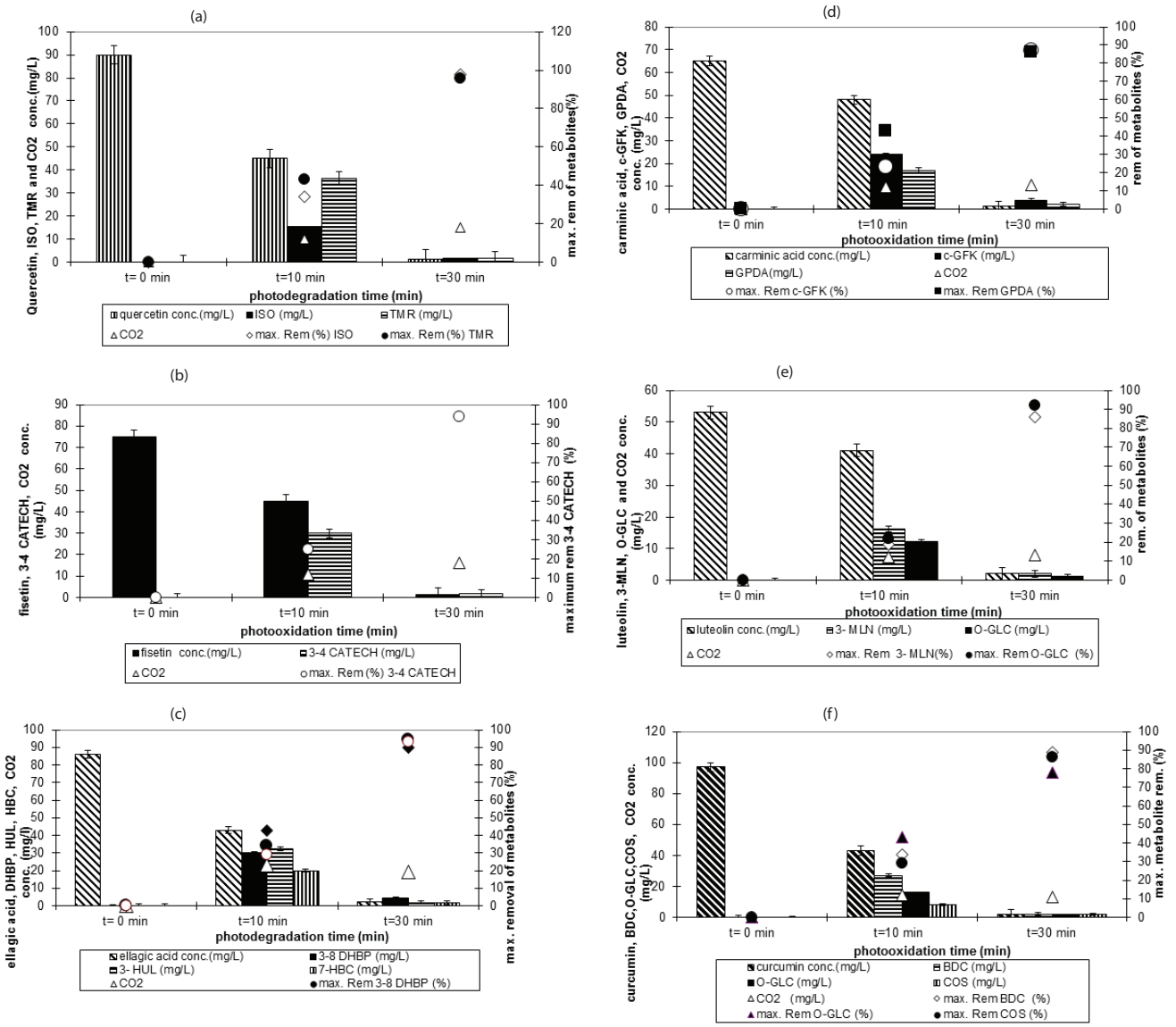

Fig. 10. Photodegradation of quercetin (a), fisetin (b), ellagic acid (c), carminic acid (d), luteolin (e) and curcumin (f) to metabolites removal under 130 W UV irradiation at original TI pH of 6.2 at a temperature of 21°C after 30 min irradiation.

enhanced with irradiation at 254 nm. Recently, Gosetti et al. [83] studied the effect of sun irradiation on carminic acid in aqueous solution. In the presence of TiO_2, they found that the carminic acid degraded under 336 nm UVA and is adsorbed to the photocatalyst TiO_2, and they reported that the photodegradatıon metabolites of carminic acid are not toxic. From 85 mg/L ellagic acid, 43 mg/L 3,8-dihydroxy-6H-dibenzopyran-6-one (3-8-DHBP), 15 mg/L 3-hydroxyurolithin (3-HUL) and 10 mg/L 7-hydroxy-3,4-benzocoumarin (7-HBC) were produced after 10 min UV irradiation (Fig. 10(b)). Ellagic acid is toxic and inhibits the TPA-induced ornithine decarboxylase activity, the hydro peroxide production and the DNA synthesis [84]. The study performed by Cerdá et al. [84] showed that 3-8-DHBP lowered the growth rate in the rats and decreased the urea and triglyceride concentrations in the blood of rats. Recent studies showed that 3-HUL and 7-HBC were produced from the hydroxylation patterns of ellagic acid by the dehydroxylase pathways in mammals, and they are not toxic to rats, to the mammals and to mice [85,86]. After 30 min UV irradiation, the ellagic acid, 3-8-DHBP, 3-HUL and 7-HBC concentrations were reduced to 4, 2, 1.8 and 1.5 mg/L, respectively, while the ellagic acid removal was 97% (Fig. 10(b)). 5 mg/L CO_2 was measured in GC–MS as the photomineralization of ellagic acid and its metabolites. Breakage of the luteolin mainly yields the moieties *O*-glucuronide (*O*-GLC) and 3′-methyl luteolin (3-MLN) as methylated isomers (Fig. 10(c)). Luteolin was found to be the most potent in inhibiting the cytokine production with an IC_{50} of less than 1 and 5 mM for a tumor necrosis factor-α (TNF-α) release [87]. After 10 min illumination with 130 W UV, at a nano-CeO_2–TiO_2 concentration of 15 mg/L, 15 mg/L 3-MLN and 12 mg/L o-GLC are two methylated metabolites of initial 53 mg/L luteolin in vivo by catechol-*O*-methyltransferase (Fig. 10(c)). The luteolin and metabiles concentrations decreased significantly with removal yields of around 96% and 98% after 30 min under UV. Although, the non-methylated luteolin showed a strong antioxidative capacity in rats [88], it was found that luteolin was cytotoxic toward H4IIE cells inducing an apoptotic cell death accompanied by induction of oxidative stress measured as an increase in malondialdehyde formation [87]. The oral LD_{50} of the lutein concentration in wistar rats was found to be greater than 2,000 mg/kg body weight [89]. Administration of the lutein concentrate to rats at doses higher than 400 mg/kg/d had adverse hematological effects. From 92 mg/L curcumin, 40 mg/L bisdemethoxycurcumin (BDC), 21 mg/L o-GLC and 6 mg/L curcumin *O*-sulfate (COS) were produced after 10 min irradiation (Fig. 10(d)). Their concentration decreased to around 2, 3, 1.6 and 0.2 mg/L after 30 min UV while as a mineralization of curcumin polyfenol and its metabolites 12 mg/L CO_2 was measured. In the literature it was found that boisduval and oviposition inhibition against female adult mites were examined under the laboratory conditions in curcumin and BDC *O*-GLC, COS metabolites [90]. BDC exhibited the highest acute toxicity to T. cinnabarinus. In other words BDC showed the highest contact toxicity (LC_{50} = 2.48 mg/mL) against adult T. cinnabarinus among the parent polyphenol and second metabolite components, whose LC_{50} values at 24 and 48 h were 1.18 and 0.51 mg/mL, respectively. Zhang et al. [91] showed that curcumin and BDC were found as potent microglia-activation inhibitors and exhibited the strongest inhibitory activity. They are cytotoxic, including TNF-α and interleukin-1β [91]. The initial quercetin concentration was 89 mg/L at the beginning of UV irradiation (Fig. 10(e)). After 10 min irradiation curcumin metabolites such as isorhamnetin (12 mg/L) and tamarixetin (TMR) (32 mg/L) were produced while the curcumin concentration was decreased to 42 mg/L (Fig. 10(f)). After 30 min UV, photodegradation products mineralized with yields around 97% and 97% while 12 mg/L CO_2 was recorded. Quercetin concentrations >1,900 mg/kg/d reduced body weight of rats in comparison with controls. After 6 months exposition toxic and neoplastic lesions were observed, but at 2 years toxic and neoplastic lesions were seen in the kidney of male rats [92]. Isorhanmetin inhibited epidermal growth factor induced neoplastic cell transformation cytotoxic activities of anagallisin; its heterogenoside was found to be weak in rats [93]. 166 nmol/mL TMR caused 97% acute toxicity to *Salmonella typhimurium* after 48 h contact time [93].

3.12. Aromatic amine and their metabolites in TI ww

The formation of possible intermediates of 2,6-DMA, MOA, TDA, NA, TOA and DCB aromatic amines is illustrated in Figs. 11(a)–(d). The intermediates of aromatic amines clearly reveal that the multiple fragmentation of aromatic amine macromolecule can lead to the complete mineralization with the end products of CO_2 and H_2O. 2,6-DMA is a nasal carcinogen and modifies the DNA in wistar rats, and it is mutagenic in the *Salmonella typhimurium* Ames assay using strain TA100 [94]. 260 mg/L initial 2,6-DMA photodegraded to 82 mg/L 4-hydroxy-2,6-dimethylaniline (4-HDA), to 41 mg/L 2-amino-3-methylbenzoic acid (2-A-3-MBA) and to 25 mg/L 2,6-dimethylnitrosobenzene (2,6 DMBN) after 10 min UV irradiation (Fig. 11(a)). The mineralization of parent 2,6-DMA occurred after 30 min with an effluent concentration of 1.2 mg/L and converted to 48 mg/L CO_2 while the concentrations of the other metabolites varied between 0.7 and 1.1 mg/L. Recent data from the National Toxicology Program reported that a principal metabolite, 4-HDA, is carcinogenic in rats. In addition, the putative metabolite *N*-hydroxy-2,6-dimethylaniline has been reported to be mutagenic in *Salmonella typhimurium* TA100 [95]. The second metabolite of 2,6-DMA is 2-A-3-MBA and does not produce hepatic lesions in the rat, except at high doses but is a potent inducer of fatty degeneration in the dog [96]. 2,6-DMBN, and the third 2,6-DMA metabolite namely nitrosodimethylamine are found to be carcinogenic activity to rats and dogs [96]. 180 mg/L initial DCB was reduced to 6 mg/L after 10 min UV irradiation, and it was photodegraded to 74 mg/L *N*-acetyl-DCB (*N*-AC-DCB) and to 42 mg/L *N*,*N*′-diacetyl-DCB (*N*,*N*-DAC-DCB). After 30 min UV the DCB and its metabolites in the effluent reduced to around 0.3–1.3 mg/L with 19 mg/L CO_2. DCB is an important intermediate in the production of diarylide azo pigments and a known animal carcinogen [97] (Fig. 11(b)). Lee et al. [98] found that 20–40 mg/kg *N*,*N*-DAC-DCB in rats resulted in dose-proportional increases in the total amount of hemoglobin after 3 weeks. *N*-AC-DCB undergoes covalent interaction with DNA, and therefore, it is suspected to be a genotoxic carcinogen [98]. 120 mg/L 3,5-aminoanisole (3,5-MOA) converted to 23 mg/L cis-l,2-dihydroxy-3-methoxycyclohexa-3,5-diene (cis-1,2-HMCH) to 60 mg/L 2-methoxyphenol (2-MOPH), to 17 mg/L catechol, and to trace amounts

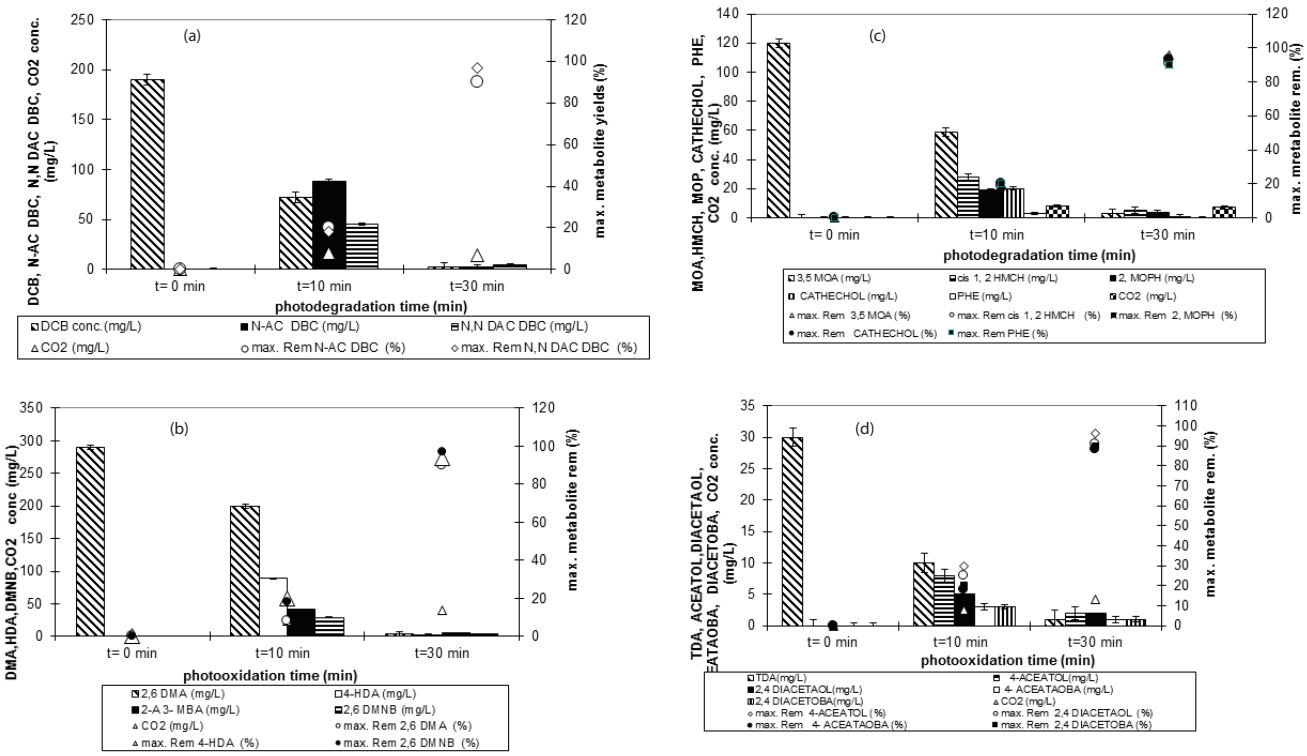

Fig. 11. Photodegradation of DBC (a), 2,6-DMA (b), 3,5-MOA (c) and TDA (d) to metabolites, and photodegradation yields of these metabolites under 130 W irradiation at 21°C and at original TI ww pH of 6.2.

of phenol (PHE) (3 mg/L) after 10 min photodegradation at 21°C with 15 mg/L CeO_2-doped TiO_2, respectively (Fig. 11(c)). After 30 min the photodegradation of parent aromatic amine and all metabolite concentrations decreased to around 0.9 and 2.4 mg/L with a CO_2 concentration of 20 mg/L. The literature studies showed that 3,5-MOA exhibited rate-limiting interactions for aquatic in vivo tests using fish, daphnids, algae and bacteria [99]. It was found that cis-1,2-HMCH is toxicity of metabolic intermediates of *Escherichia coli* JM109 [100]. Schweigert et al. [101] reported that as a consequence of the chemical properties and the chemical reactions of catechols, many different reactions can occur with biomolecules such as DNA, proteins and membranes, ultimately leading to non-repairable damage. 2-MOPH and PHE are not toxic and are readily biodegradable as low as 0.001 mg/L concentrations. Thompson et al. [102] found that 2-MOPH is more toxic in rat liver slices. 28 mg/L initial TDA photodegraded to 8.25 mg/L 4-acetylamino-2-aminotoluene (4-ACETOL) to 4.5 mg/L 2,4-diacetylaminotoluene (2,4 DIACETAOL), to 2.45 mg/L 4-acetylamino-2-aminobenzoic acid (4-ACEATOBA), and to 2.51 mg/L 2,4-diacetylaminobenzoic acid (2,4 DIACETOBA)) after 10 min irradiation times at 130 W UV power (Fig. 11(d)). Acute toxicity of 2,4- DIACETOBA is LD_{50} = 2,850 mg/kg/d [102].

4. Conclusions

The particle size of CeO_2-doped TiO_2 nanocomposite synthesized under laboratory conditions increased to 265 nm compared with single TiO_2 (198.4 nm) and CeO_2 (86.2 nm), and exhibited a mesoporous texture. CeO_2 exhibited cubic-fluorite phase in band at 460 cm^{-1} while at band 595 cm^{-1} oxygen vacancies in the CeO_2 lattice was detected. 15 mg/L CeO_2-doped TiO_2 nanocomposite with a CeO_2 ratio of 15 wt% showed the highest photodegradation yield of color (98%), polyphenol (quercetin, fisetin, ellagic acid, carminic acid, luteolin, and curcumin; 98%) and polyaromatic amine (2,6-DMA, MOA, TDA, TOA and DCB- 98%) photodegradation rates, respectively, after 30 min irradiation time at a UV power of 130 W at a pH = 6.2. The photodegradation yields of metabolites of polyphenols (quercetin, fisetin, ellagic acid, carminic acid, luteolin, and curcumin) and polyaromatics (2,6-DMA, MOA, TDA, TOA and DCB) varied between 96% and 99%.

Acknowledgment

This research study was undertaken in the Environmental Microbiology Laboratory at Dokuz Eylül University Engineering Faculty Environmental Engineering Department, İzmir, Turkey. The authors would like to thank this body for providing financial support.

References

[1] E.H. Robinson, M.H. Li, B.B. Manning, Evaluation of corn gluten feed as a dietary ingredient for pond-raised channel catfish *Ictalurus punctatus*, J. World Aquacult. Soc., 32 (2001) 68–71.

[2] H. Keharia, D. Madamwar, Bioremediation concept for treatment of dye containing wastewater: a review, Indian J. Exp. Biol., 41 (2003) 1068–1075.

[3] A.A. Khan, Q. Husain, Decolorization and removal of textile and non-textile dyes from polluted wastewater and dyeing effluent by using potato (*Solanum tuberosum*) soluble and immobilized polyphenol oxidase, Bioresour. Technol., 98 (2007) 1012–1019.
[4] R.G. Saratale, G.D. Saratale, J.S. Chang, S.P. Govindwar, Bacterial decolorization and degradation of azo dyes: a review, J Taiwan Inst. Chem. Eng., 42 (2011) 138–157.
[5] R.V. Khandare, S.P. Govindwar, Phytoremediation of textile dyes and effluents: current scenario and future prospects, Biotechnol. Adv., 33 (2015) 1697–1714.
[6] S.K. Garg, A. Kalla, A. Bhatnagar, Evaluation of raw and hydrothermically processed leguminous seeds as supplementary feed for the growth of two Indian major carp species, Aquacult. Res., 33 (2002) 151–163.
[7] IARC Monographs on the Evaluation of the Carcinogenic Risk of Chemicals to Humans, Vol. 100, 1982.
[8] S.V. Sharma, D.W. Bell, J. Settleman, D.A. Haber, Epidermal growth factor receptor mutations in lung cancer, Nat. Rev. Cancer, 7 (2007) 69–81.
[9] S. Jadhav, V. Gulati, E.M. Fox, A. Karpe, D.J. Beale, D. Sevior, M. Bhave, E.A. Palombo, Rapid identification and source-tracking of Listeria monocytogenes using MALDITOF mass spectrometry, Int. J. Food Microbiol., 202 (2015) 1–9.
[10] S. Yesiladali, P. Gulseren, B. Hakan, A. Idil, O. Derin, T. Candan, Bioremediation of textile azo dyes by *Trichophyton rubrum* LSK-27, World J. Microbiol. Biotechnol., 22 (2006) 1027–1031.
[11] U. Asghar, M.T. Herrera-Abreu, R. Cutts, I. Babina, A. Pearson, N.C. Turner, Identification of subtypes of triple negative breast cancer (TNBC) that are sensitive to CDK4/6 inhibition, J. Clin. Oncol., 33 (2015) 11098.
[12] K. Sarayu, S. Sandhya, Rotating biological contactor reactor with biofilm promoting mats for treatment of benzene and xylene containing wastewater, Appl. Biochem. Biotechnol., 168 (2012) 1928–1937.
[13] J.-S. Bae, H.S. Freeman, Aquatic toxicity evaluation of new direct dyes to the *Daphnia magna*, Dyes Pigm., 73 (2007) 81–85.
[14] D.P. Edwards, L.K. Emmons, D.A. Hauglustaine, D.A. Chu, J.C. Gille, Y.J. Kaufman, G. Pétron, L.N. Yurganov, L. Giglio, M.N. Deeter, V. Yudin, D.C. Ziskin, J. Warner, J.-F. Lamarque, G.L. Francis, S.P. Ho, D. Mao, J. Chen, E.I. Grechko, J.R. Drummond, Observations of carbon monoxide and aerosols from the Terra satellite: Northern Hemisphere variability, J. Geophys. Res., 109 (2004) D24202.
[15] E.K. Lee, R.J. Gallagher, D.A. Patterson, A linear programming approach to discriminant analysis with a reserved judgment region, INFORMS J. Comput., 15 (2003) 23–41.
[16] Q. Fu, S. Manabe, C.M. Johanson, On the warming in the tropical upper troposphere: models versus observations, Geophys. Res. Lett., 38 (2011) 1–6.
[17] A. Choughule, R. Sharma, V. Trivedi, A. Thavamani, V. Noronha, A. Joshi, S. Desai, P. Chandrani, P. Sundaram, S. Utture, N. Jambhekar, S. Gupta, J. Aich, K. Prabhash, A. Dutt, Coexistence of *KRAS* mutation with mutant but not wild-type *EGFR* predicts response to tyrosine-kinase inhibitors in human lung cancer, Br. J. Cancer, 111 (2014) 2203–2204.
[18] M. Işik, D.T. Sponza, Fate and toxicity of azo dye metabolites under batch long-term anaerobic incubations, Enzyme Microb. Technol., 40 (2007) 934–939.
[19] A. Klepacz-Smółka, J. Sójka-Ledakowicz, S. Ledakowicz, Biological treatment of post-nanofiltration concentrate of real textile wastewater, Fibres Text. East. Eur., 23 (2015) 138–143.
[20] G. Eremektar, H. Selcuk, S. Meric, Investigation of the relation between COD fractions and the toxicity in a textile finishing industry wastewater: effect of preozonation, Desalination, 211 (2007) 314–320.
[21] X.H. Ning, N. Zhang, T. Li, P.J. Wu, X. Wang, X.Y. Li, S.H. Peng, J.Y. Wang, J.C. Chen, K. Gong, Telomere shortening is associated with genetic anticipation in Chinese Von Hippel-Lindau disease families, Cancer Res., 74 (2014) 3802–3809.
[22] F.P. van der Zee, S. Villaverde, Combined anaerobic–aerobic treatment of azo dyes—a short review of bioreactor studies, Water Res., 39 (2005) 1425–1440.
[23] J. Li, S. Saxena, D. Pain, A. Dancis, Adrenodoxin reductase homolog (Arh1p) of yeast mitochondria required for iron homeostasis, J. Biol. Chem., 276 (2001) 1503–1509.
[24] M. Porru, S. Zappavigna, G. Salzano, A. Luce, A. Stoppacciaro, M.L. Balestrieri, S. Artuso, S. Lusa, G. De Rosa, C. Leonetti, M. Caraglia, Medical treatment of orthotopic glioblastoma with transferrin-conjugated nanoparticles encapsulating zoledronic acid, Oncotarget, 5 (2014) 10446–10459.
[25] E.L. Greer, M.A. Blanco, L. Gu, E. Sendinc, J. Liu, D. Aristizábal-Corrales, C.H. Hsu, L. Aravind, C. He, Y. Shi, DNA methylation on N6-adenine in *C. elegans*, Cell, 161 (2015) 868–878.
[26] The World Bank, The Annual Report, 2015.
[27] T. Kawakami, M. Kuzoki, M. Iskii, Y. Igarashi, H. Arai, Differential expression of multiple terminal oxidases for aerobic respiration in *Pseudomonas aeruginosa*, Environ. Microbiol., 12 (2010) 1399–1412.
[28] P. Møller, H. Wallin, Genotoxic hazards of azo pigments and other colorants related to 1-phenylazo-2-hydroxynaphthalene, Mutat. Res., 462 (2000) 13–30.
[29] R.C. Lima, M.F.F. Fuentes, E.R. Freitas, F.S. Sucupira, R.F. Moreira, N.M. Braz, Coconut meal in laying hens diets: nutrients digestibility, performance and egg quality, Rev. Bras. Zootec., 36 (2007) 1340–1346.
[30] OECD's 2004 Review of the US Economy Examines the Key Challenges the US Faces for Sustaining Economic Growth, OECD Publishing, 198, ISBN: 9789264015807, 2004.
[31] European Company, Council Regulation (EC) No 1435/2003 of 22 July 2003 on the Statute for a European Cooperative Society (SCE), OJ L 207, 2003, pp. 1–24.
[32] R.S. Ellis, M. Colless, T. Broadhurst, J. Heyl, K. Glazebrook, Autofib redshift survey I. Evolution of the galaxy luminosity function, Mon. Not. R. Astron. Soc., 280 (1996) 235.
[33] I.K. Kapdan, R. Oztekin, The effect of hydraulic residence time and initial COD concentration on color and COD removal performance the anaerobic–aerobic SBR system, J. Hazard. Mater., 136 (2006) 896–901.
[34] M. Azizi, M. Sapoval, P. Gosse, M. Monge, G. Bobrie, P. Delsart, M. Midulla, C. Mounier-Véhier, P.-Y. Courand, P. Lantelme, T. Denolle, C. Dourmap-Collas, H. Trillaud, H. Pereira, P.-F. Plouin, G. Chatellier, Optimum and stepped care standardised antihypertensive treatment with or without renal denervation for resistant hypertension (DENERHTN): a multicentre, open-label, randomised controlled trial, Lancet, 385 (2015) 1957–1965.
[35] D.T. Sponza, M. Işık, Decolorization and azo dye degradation by anaerobic/aerobic sequential process, Enzyme Microb. Technol., 31 (2002) 102–110.
[36] U.B. Pandey, Z. Nie, Y. Batlevi, B.A. McCray, G.P. Ritson, N.B. Nedelsky, S.L. Schwartz, N.A. DiProspero, M.A. Knight, O. Schuldiner, R. Padmanabhan, M. Hild, D.L. Berry, D. Garza, C.C. Hubbert, T.P. Yao, E.H. Baehrecke, J.P. Taylor, HDAC6 rescues neurodegeneration and provides an essential link between autophagy and the UPS, Nature, 447 (2007) 859–863.
[37] S. Popli, U.D. Patel, Destruction of azo dyes by anaerobic–aerobic sequential biological treatment: a review, Int. J. Environ. Sci. Technol., 12 (2015) 405–420.
[38] S.D.N. Lourenço, D. Gallipoli, D.G. Toll, E.D. Evans, Development of Commercial Tensiometer for Triaxial Testing of Unsaturated Soils, Proc. 4th International Conference on Unsaturated Soils, Vol. 2, Arizona, USA, 2006, pp. 1875–1886.
[39] S. Esplugas, P.L. Yue, M.I. Pervez, Degradation of 4-chlorophenol by photolytic oxidation, Water Res., 28 (1994) 1323–1328.
[40] S.J. Masten, S.H.R. Davies, The use of ozonation to degrade organic contaminants in wastewaters, Environ. Sci. Technol., 28 (1994) 180A–185A.
[41] M. Besson, C. Descorme, M. Bernardi, P. Gallezot, F. Di Gregorio, N. Grosjean, D. Pham Minh, A. Pintar, Supported noble metal catalysts in the catalytic wet air oxidation of industrial wastewaters and sewage sludges, Environ. Technol., 31 (2010) 1441–1447.
[42] X.B. Chen, S.S Mao, Titanium dioxide nanomaterials: synthesis, properties, modifications, and applications, Chem. Rev., 107 (2007) 2891–2959.

[43] R. Jain, S. Sikarwar, Semiconductor-mediated photocatalyzed degradation of erythrosine dye from wastewater using TiO_2 catalyst, Environ. Technol., 31 (2010) 1403–1410.
[44] H.R. Pouretedal, H. Beigy, M.H. Keshavarz, Bleaching of Congo red in the presence of ZnS nanoparticles, with dopant of CO^{2+} ion, as photocatalyst under UV and sunlight irradiations, Environ. Technol., 31 (2010) 1183–1190.
[45] M.S. Vohraa, S.M. Selimuzzaman, M.S. Al-Suwaiyan, NH_4^+-NH_3 removal from simulated wastewater using UV, TiO_2 photocatalysis: effect of co-pollutants and pH, Environ. Technol., 31 (2010) 641–654.
[46] A.L. Linsebigler, G. Lu, J.T. Yates, Photocatalysis on TiO_2 surfaces: principles, mechanisms, and selected results, Chem. Rev., 95 (1995) 735–758.
[47] Y. Zheng, E. Shi, Z. Chen, W. Li, X. Hu, Influence of solution concentration on the hydrothermal preparation of titania crystallites, J. Mater. Chem., 11 (2001) 1547–1551.
[48] H. Yamashita, H. Harada, J. Misaka, M. Takeushi, K. Ikeue, M. Anpo, Degradation of propanol diluted in water under visible light irradiation using metal ion-implanted titanium dioxide photocatalysts, J. Photochem. Photobiol., A, 148 (2002) 257–261.
[49] J.C. Yu, L. Zhang, Z. Zheng, J. Zhao, Synthesis and characterization of phosphated mesoporous titanium dioxide with high photocatalytic activity, Chem. Mater., 15 (2003) 2280–2286.
[50] W. Wang, J. Zhang, F. Chen, D. He, M. Anpo, Preparation and photocatalytic properties of Fe^{3+}-doped Ag@TiO_2 core–shell nanoparticles, J. Colloid Interface Sci., 323 (2008) 182–186.
[51] F. Chen, W. Zou, W. Qu, J. Zhang, Photocatalytic performance of a visible light TiO_2 photocatalyst prepared by a surface chemical modification process, Catal. Commun., 10 (2009) 1510–1513.
[52] S.K. Bhargava, J. Tardio, J. Prasad, K. Főger, D.B. Akolekar, S.C. Grocatt, Wet oxidation and catalytic wet oxidation, Ind. Eng. Chem. Res., 45 (2006) 1221–1258.
[53] P. Massa, F. Ivorra, P. Haure, F. Medina Cabello, R. Fenoglio, Catalytic wet air oxidation of phenol aqueous solutions by 1% Ru/CeO_2–Al_2O_3 catalysts prepared by different methods, Catal. Commun., 8 (2007) 424–428.
[54] S. Pavasupree, Y. Suzuki, S. Pivsa-Art, S. Yoshikawa, Preparation and characterization of mesoporous TiO_2–CeO_2 nanopowders respond to visible wavelength, J. Solid State Chem., 178 (2005) 128–134.
[55] T. Morimo, G. Dutta, U.V. Waghmare, T. Baidya, M.S. Hegde, K.R. Priolkar, P.R. Sarode, Origin of enhanced reducibility/oxygen storage capacity of $Ce_{1-x}Ti_xO_2$ compared to CeO_2 or TiO_2, Chem. Mater., 18 (2006) 3249–3256.
[56] G. Li, D. Zhang, J.C. Yu, Thermally stable ordered mesoporous CeO_2/TiO_2 visible-light photocatalysts, Phys. Chem. Chem. Phys., 11 (2009) 3775–3782.
[57] Y. Zhang, J. Ling, C. Yuan, R. Dubruille, P. Emery, A role for Drosophila ATX2 in activation of PER translation and circadian behavior, Science, 340 (2013) 879–882.
[58] A. Pirkarami, M.E. Olya, S.R. Farshid, UV/Ni–TiO_2 nanocatalyst for electrochemical removal of dyes considering operating costs, Water Resour. Ind., 5 (2014) 9–20.
[59] X. Shao, W. Lu, R. Zhang, F. Feng Pan, Enhanced photocatalytic activity of TiO_2-C hybrid aerogels for methylene blue degradation, Sci. Rep., 3 (2013) 1–9. doi: 10.1038/srep03018.
[60] A. Besson, H.C. Hwang, S. Cicero, S.L. Donovan, M. Gurian-West, D. Johnson, B.E. Clurman, M.A. Dyer, J.M. Roberts, Discovery of an oncogenic activity in $p27^{Kip1}$ that causes stem cell expansion and a multiple tumor phenotype, Genes Dev., 21 (2007) 1731–1746.
[61] P. Ji, B. Tian, F. Chen, J. Zhang, CeO_2 mediated photocatalytic degradation studies of C.I. acid orange 7, Environ. Technol., 33 (2012) 467–472.
[62] H. Balavi, S. Samadanian-Isfahani, M. Mehrabani-Zeinabad, M. Edrissi, Preparation and optimization of CeO_2 nanoparticles and its application in photocatalytic degradation of Reactive Orange 16 dye, Powder Technol., 249 (2013) 549–555.
[63] B. Zhao, B. Shi, X. Zhang, X. Cao, Y. Zhang, Catalytic wet hydrogen peroxide oxidation of H-acid in aqueous solution with, TiO_2–CeO_2 and Fe/TiO_2–CeO_2 catalysts, Desalination, 268 (2011) 55–59.
[64] H. Liu, M. Wang, Y. Wang, Y. Liang, W. Cao, Y. Su, Ionic liquid-templated synthesis of mesoporous CeO_2–TiO_2 nanoparticles and their enhanced photocatalytic activities under UV or visible light, J. Photochem. Photobiol., A., 223 (2011) 157–164.
[65] S. Ameen, M.S. Akhtar, H.-K. Seo, H.-S. Shin, Solution-processed CeO_2/TiO_2 nanocomposite as potent visible light photocatalyst for the degradation of bromophenol dye, Chem. Eng. J., 247 (2014) 193–198.
[66] M. Li, S. Zhang, L. Lv, M. Wang, W. Zhang, B. Pan, A thermally stable mesoporous ZrO_2–CeO_2–TiO_2 visible light photocatalyst, Chem. Eng. J., 229 (2013) 118–125.
[67] Z. Shi, P. Yang, F. Tao, R. Zhou, New insight into the structure of CeO_2–TiO_2 mixed oxides and their excellent catalytic performances for 1,2-dichloroethane oxidation, Chem. Eng. J., 295 (2016) 99–108.
[68] A.D. Eaton, L.S. Clesceri, E.W. Rice, A.E. Greenberg, M.A.H. Franson, Standard Methods for the Examination of Water and Wastewater, 21st ed., American Public Health Association (APHA), American Water Works Association (AWWA), Water Environment Federation (WEF), Washington, D.C., USA, 2005.
[69] Y. Wang, J. Zhao, T. Wang, Y. Li, X. Li, J. Yin, C. Wang, CO_2 photoreduction with H_2O vapor on highly dispersed CeO_2/TiO_2 catalysts: surface species and their reactivity, J. Catal., 337 (2016) 293–302.
[70] M.J. Muñoz-Batista, M.N. Gómez-Cerezo, A. Kubacka, D. Tudela, M. Fernández-García, Role of interface contact in CeO_2–TiO_2 photocatalytic composite materials, ACS Catal., 4 (2014) 63–72.
[71] C. Karunakaran, P. Gomathisankar, Solvothermal synthesis of CeO_2–TiO_2 nanocomposite for visible light photocatalytic detoxification of cyanide, ACS Sustainable Chem. Eng., 1 (2013) 1555–1563.
[72] J. Santiago-Morales, A. Aguera, M.M. Gomez, A.R. Fernandez-Alba, J. Gimeno, S. Esplugas, R. Rosal, Transformation products and reaction kinetics in simulated solar light photocatalytic degradation of propranolol using Ce doped TiO_2, Appl. Catal., B, 129 (2013) 13–29.
[73] S. Ghasemi, S. Rahman Setayesh, A. Habibi-Yangjeh, M.R. Hormozi-Nezhad, M.R. Gholami, Assembly of CeO_2–TiO_2 nanoparticles prepared in room temperature ionic liquid on graphene nanosheets for photocatalytic degradation of pollutants, J. Hazard. Mater., 199–200 (2012) 170–178.
[74] M.E. Contreras-Garcíaa, M.L García-Benjume, V.I. Macías-Andrésa, E. Barajas-Ledesma, A. Medina-Floresa, M.I. Espitia-Cabrerac, Synergic effect of the TiO_2-CeO_2 nanoconjugate system on the band-gap for visible light photocatalysis, Mater. Sci. Eng., B, 183 (2014) 78–85.
[75] S. Watanabe, X. Ma, C. Song, Characterization of structural and surface properties of nanocrystalline TiO_2–CeO_2 mixed oxides by XRD, XPS, TPR, and TPD, J. Phys. Chem. C, 113 (2009) 14249–14257.
[76] J. Qian, Z. Chen, C. Liu, X. Lu, F. Wang, M. Wang, Improved visible-light-driven photocatalytic activity of CeO_2 microspheres obtained by using lotus flower pollen as biotemplate, Mater. Sci. Semicond. Process., 25 (2014) 27–33.
[77] J. Fang, X. Bi, D. Si, Z. Jiang, W. Huang, Spectroscopic studies of interfacial structures of CeO_2–TiO_2 mixed oxides, Appl. Surf. Sci., 253 (2007) 8952–8961.
[78] H. Wen, Z. Liu, Q. Yang, Y. Li, J. Yu, Synthesis and electrochemical properties of CeO_2 nanoparticle modified TiO_2 nanotube arrays, Electrochim. Acta, 56 (2011) 2914–2918.
[79] Y. Yu, X. Yu, S. Yang, Preparation and characterization of CeO_2 decorated TiO_2 nanotube arrays photoelectrode and its enhanced photoelectrocatalytic efficiency for degradation of methyl orange, J. Mater Sci. - Mater. Electron., 26 (2015) 5715–5723.
[80] W. Brack, R. Altenburger, E. Küster, B. Meissner, K.D. Wenzel, G. Schüürmann, Identification of toxic products of anthracene photomodification in simulated sunlight, Environ. Toxicol. Chem., 22 (2003) 2228–2237.
[81] R. Sarikaya, M. Selvi, F. Erkoç, Evaluation of potential genotoxicity of five food dyes using the somatic mutation and recombination test, Chemosphere, 88 (2012) 974–979.

[82] K. Jørgensen, L.H. Skibsted, Light sensitivity of cochineal. Quantum yields for photodegradation of carminic acid and conjugate bases in aqueous solution, Food Chem., 40 (1991) 25–34.
[83] F. Gosetti, E. Mazzucco, M.C. Gennaro, E. Marengo, Contaminants in water: non-target UHPLC/MS analysis, Envion. Chem. Lett., 14 (2016) 51–65.
[84] B. Cerdá, R. Llorach, J.J. Ceròn, J.C. Espìn, F.A. Tomàs-Barberàn, Evaluation of the bioavailability and metabolism in the rat of punicalagin, an antioxidant polyphenol from pomegranate juice, Eur. J. Nutr., 42 (2003) 18–28.
[85] T.N. Kopylova, L.G. Samsonova, R.M. Gadirov, V.P. Khilya, V.V. Ishchenko, O.V. Shablykina, The Nature of the Photoprocesses in the New 7-Hydroxycoumarines, Proc. SPIE 6938, Atomic and Molecular Pulsed Lasers VII, Vol. 6938, 2008. doi:10.1117/12.785624.
[86] R. González-Barrio, P. Truchado, H. Ito, J.C. Espín, F.A. Tomás-Barberán, UV and MS identification of urolithins and nasutins, the bioavailable metabolites of ellagitannins and ellagic acid in different mammals, J. Agric. Food Chem., 59 (2011) 1152–1162.
[87] B.A. Michel, G. Stucki, D. Frey, F. De Vathaire, E. Vignon, P. Bruehlmann, D. Uebelhart, Chondroitins 4 and 6 sulfate in osteoarthritis of the knee: a randomized, controlled trial, Arthritis Rheum. 52 (2005) 779–786.
[88] A. Xagorari, A. Papapetropoulos, A. Mauromatis, M. Economou, T. Fotsis, C. Roussos, Luteolin inhibits an endotoxin-stimulated phosphorylation cascade and proinflammatory: cytokine production in macrophages, J. Pharmacol. Exp. Ther., 296 (2001) 181–187.
[89] R. Ravikrishnan, S. Rusia, G. Ilamurugan, U. Salunkhe, J. Deshpande, J. Shankaranarayanan, M.L. Shankaranarayana, M.G. Soni, Safety assessment of lutein and zeaxanthin (Lutemax™ 2020): subchronic toxicity and mutagenicity studies, Food Chem. Toxicol., 49 (2011) 2841–2848.
[90] Z.Y. Qiang, D. Wei, Z. Zhimo, Biological activities of curcuminoids against *Tetranychus cinnabarinus* Boisduval (Acari: Tetranychidae) (cba:647484), Neurosci. Lett., 447 (2008) 48–53.
[91] L.J. Zhang, C.F. Wu, X.L. Meng, D. Yuan, X.D. Cai, Q.L. Wang, J.Y. Yang, Comparison of inhibitory potency of three different curcuminoid pigments on nitric oxide and tumor necrosis factor production of rat primary microglia induced by lipopolysaccharide, Neurosci. Lett., 447 (2008) 48–53.
[92] J.K. Dunnick, J.R. Hailey, Toxicity and carcinogenicity studies of quercetin, a natural component of foods, Fundam. Appl. Toxicol., 19 (1992) 423–431.
[93] International Organization for Standardization, ISO 9001, Quality Management Systems – Requirements, 3rd ed., ICS: 03.120.10 Quality Management and Quality Assurance, 03.100.70 Management Systems, Technical Committee: ISO/TC 176/SC 2 Quality Systems, 2000.
[94] A.M. Jeffrey, F.-Q. Luo, S. Amin, J. Krzeminski, K. Zech, G.M. Williams, Lack of DNA binding in the rat nasal mucosa and other tissues of the nasal toxicants roflumilast, a phosphodiesterase 4 inhibitor, and a metabolite, 4-amino-3,5-dichloropyridine, in contrast to the nasal carcinogen 2,6-dimethylaniline, Drug Chem. Toxicol., 25 (2002) 93–107.
[95] M.S. Bryant, H.F. Simmons, R.E. Harrell, J.A. Hinson, 2,6-Dimethylaniline—hemoglobin adducts from lidocaine in humans, Carcinogenesis, 15 (1994) 2287–2290.
[96] C.R. Short, M.L. Hardy, S.A. Barker, The in vivo oxidative metabolism of 2,4- and 2,6-dimethylaniline in the dog and rat, Toxicology, 57 (1989) 45–58.
[97] J.H. Lee, H.S. Shin, Determination of hemoglobin adducts formed in rats exposed orally with 3,3′-dichlorobenzidine by GC/MS-SIM, Toxicol. Ind. Health, 18 (2002) 191–199.
[98] J.-H. Lee, H.-S. Shin, D.-G. Jung, Y.-S. Lee, Urinary monitoring method of 3,3′-dichlorobenzidine (DCB) and its metabolites, N-acetyl-DCB and N,N′-diacetyl-DCB, Ind. Health, 41 (2003) 242–248.
[99] M. Nendza, A. Wenzel, Discriminating toxicant classes by mode of action. 1. (Eco)toxicity profiles, Environ. Sci. Pollut. Res. Int., 13 (2006) 192–203.
[100] R.J. Swift, S.F. Carter, D.A. Widdowson, J.R. Mason, D.J. Leak, Expression of benzene dioxygenase from *Pseudomonas putida* ML2 in cis-1,2-cyclohexanediol-degrading pseudomonads, Appl. Microbiol. Biotechnol., 55 (2001) 721–726.
[101] N. Schweigert, A.J. Zehnder, R.I. Eggen, Chemical properties of catechols and their molecular modes of toxic action in cells, from microorganisms to mammals, Environ. Microbiol., 3 (2001) 81–91.
[102] D.C. Thompson, K. Perera, E.S. Krol, J.L. Bolton, o-Methoxy-4-alkylphenols that form quinone methides of intermediate reactivity are the most toxic in rat liver slices, Chem. Res. Toxicol., 8 (1995) 323–327.